

Projections from neocortex mediate top-down control of memory retrieval

Priyamvada Rajasethupathy^{1,2*}, Sethuraman Sankaran^{2*}, James H. Marshel^{1*}, Christina K. Kim^{1,3}, Emily Ferenczi^{1,3}, Soo Yeun Lee^{1,3}, Andre Berndt^{1,3}, Charu Ramakrishnan¹, Anna Jaffe¹, Maisie Lo¹, Conor Liston^{1,4} & Karl Deisseroth^{1,2,4,5}

Top-down prefrontal cortex inputs to the hippocampus have been hypothesized to be important in memory consolidation, retrieval, and the pathophysiology of major psychiatric diseases; however, no such direct projections have been identified and functionally described. Here we report the discovery of a monosynaptic prefrontal cortex (predominantly anterior cingulate) to hippocampus (CA3 to CA1 region) projection in mice, and find that optogenetic manipulation of this projection (here termed AC-CA) is capable of eliciting contextual memory retrieval. To explore the network mechanisms of this process, we developed and applied tools to observe cellular-resolution neural activity in the hippocampus while stimulating AC-CA projections during memory retrieval in mice behaving in virtual-reality environments. Using this approach, we found that learning drives the emergence of a sparse class of neurons in CA2/CA3 that are highly correlated with the local network and that lead synchronous population activity events; these neurons are then preferentially recruited by the AC-CA projection during memory retrieval. These findings reveal a sparsely implemented memory retrieval mechanism in the hippocampus that operates via direct top-down prefrontal input, with implications for the patterning and storage of salient memory representations.

Pioneering studies (recently reviewed¹) have illuminated the molecular and physiological mechanisms of information storage at synapses, but how populations of individual neurons form network representations of memory is largely unknown. Recent studies have reported that only a fraction of eligible neurons are allocated during learning to form a memory^{2–4}, that the population initially encoding the memory is later preferentially recruited during retrieval of that memory⁵, and that subsequent activation of the initial ensemble alone can be sufficient for memory retrieval^{6–8}. Intriguing questions remain regarding (for instance) whether neurons in the memory ensemble have different roles in storage and retrieval, or are controlled by top-down influences^{9–11} distinct from the well-explored bottom-up entorhinal/hippocampal system; such top-down prefrontal projections to the hippocampus (if functionally present) might also support bidirectional communication during memory consolidation¹², and would potentially be relevant to psychiatric disorders such as post-traumatic stress disorder¹³, schizophrenia¹⁴ and drug addiction¹⁵. It is also unclear whether behaviourally salient memories are laid down broadly across the brain^{16,17}, or are wired topographically within the local network for improved access^{18–21}. To address these and other questions regarding real-time population-level mechanisms of memory storage and retrieval, we developed an approach to visualize and perturb top-down modulation of rapidly evolving memory ensembles in behaving mammals.

AC-CA: a direct top-down projection

To identify direct top-down inputs to the hippocampus, we injected a retrograde tracer capable of labelling afferent neurons with tdTomato (RV-tdT²²) into the hippocampus. We observed robust tdT labelling in brain regions with known inputs to the hippocampus, including the medial septum, contralateral CA3 and entorhinal cortex (Fig. 1a and Extended Data Fig. 1a). Additionally, we identified a previously

uncharacterized input arising from the dorsal anterior cingulate cortex (AC) and adjacent frontal cortical association cortex, both of which are reciprocally connected with the mediodorsal thalamic nucleus—a defining feature of the prefrontal cortex (PFC) in rodents (Fig. 1a; also confirmed with another retrograde tracer, canine adenovirus (CAV)²³; Extended Data Fig. 1b). Injection of RV-tdT in the AC also sparsely labelled neurons bilaterally in the dorsal hippocampus, consistent with potential bidirectional communication between the AC and hippocampus (Extended Data Fig. 1c). To validate further the existence of this novel PFC-to-hippocampus projection, we injected an anterograde label (adeno-associated virus 5-enhanced yellow fluorescent protein (AAV5-eYFP)) into the dorsal AC (Fig. 1b) and detected fluorescence-filled projection terminals bilaterally in the striatum and ipsilaterally in the medial dorsal thalamic nucleus (both areas are known to receive projections from the PFC), but also bilaterally in the hippocampus.

To determine if these prefrontal projections gave rise to direct monosynaptic drive of hippocampal neurons, we transduced the AC with an AAV encoding a channelrhodopsin (ChR), and performed patch-clamp recordings of light-driven excitatory postsynaptic currents (EPSCs) in CA1/CA3 cell bodies (Fig. 1c). Cells in both CA1 (Fig. 1d) and CA3 (Fig. 1f) reliably responded to light pulse trains, and generated evoked EPSC amplitudes sufficient to drive action potentials (Fig. 1h, i). Responses when present were fast, with mean latency of 3.2 ms in CA1 ($n = 26$; Fig. 1e) and 2.7 ms in CA3 ($n = 13$; Fig. 1g); along with the observation of sustained evoked spikes after 10 Hz stimulation (Fig. 1h, i), this finding was consistent with the presence of a direct and efficacious monosynaptic connection from the AC onto hippocampal pyramidal cells in the CA3/CA1 subfields, which we accordingly term the AC-CA projection. No responses were observed in dentate neurons (Fig. 1j).

¹Department of Bioengineering, Stanford University, Stanford, California 94305, USA. ²CNC Program, Stanford University, Stanford, California 94305, USA. ³Neuroscience Program, Stanford University, Stanford, California 94305, USA. ⁴Department of Psychiatry and Behavioral Sciences, Stanford University, Stanford, California 94305, USA. ⁵Howard Hughes Medical Institute, Stanford University, Stanford, California 94305, USA.

*These authors contributed equally to this work.

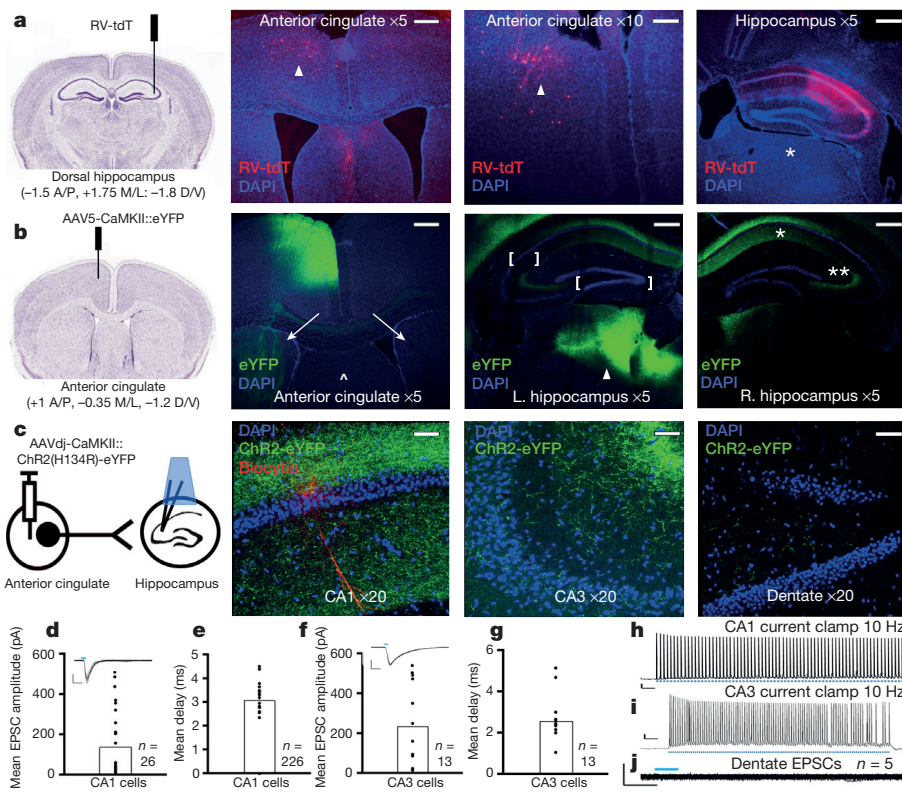


Figure 1 | Characterization of AC-CA monosynaptic projection. **a**, Five days after RV-tdT injection into the hippocampus (coordinates specified), retrogradely labelled neurons were detected in the AC (arrowhead). The injection did not leak below the hippocampus into the medial dorsal thalamus (asterisk), a known projection target of the PFC. Scale bars: $\times 5$: 300 μ m; $\times 10$: 100 μ m (confocal). A, anterior; D, dorsal; DAPI, 4',6-diamidino-2-phenylindole; M, medial; L, lateral; V, ventral. **b**, Five weeks after AAV5-CaMKII::eYFP injection into the AC (coordinates specified), projection fibres were visualized in the bilateral striatum (arrows), the bilateral hippocampus at the stratum oriens and stratum radiatum of CA1 (one asterisk) and CA3 (two asterisks), and the ipsilateral medial dorsal thalamus (arrowhead), while

sparing CA2 and the dentate (brackets). The injection did not leak into the medial septum, a known input to the hippocampus (caret). Scale bars: $\times 5$: 300 μ m (100 μ m maximum projections). L, left; R, right. **c**, AAVdj-CaMKII::ChR2(H134R)-eYFP was injected into the dorsal AC; post-synaptic responses were recorded from CA1 pyramids in acute slice. Scale bars: $\times 20$: 60 μ m. **d**, CA1 response amplitudes ($n = 26$ neurons, $n = 6$ mice); inset: raw traces. **e**, CA1 response latency (mean 3.2 ms). **f**, CA3 response amplitudes ($n = 13$ neurons, $n = 2$ mice); inset: raw traces. **g**, CA3 response latency (mean 2.7 ms). **h**, **i**, CA1 (**h**) and CA3 (**i**) current-clamp traces illustrating spiking reliability at 10 Hz. Scale: 10 mV, 250/500 ms. **j**, No responses were detected in dentate neurons ($n = 5$).

AC-CA: causal role in memory retrieval

To probe the functional importance of this projection, we conducted a series of optogenetic experiments to manipulate this pathway before and after contextual fear conditioning, and also in the setting of memory extinction and reinstatement. We first injected RV-ChR2-eYFP (or RV-eYFP) into the dorsal hippocampus, and targeted light delivery to retrogradely labelled cell bodies in the AC (Extended Data Fig. 2a). On day 1, ChR2 and eYFP mice underwent contextual fear conditioning in one context, while a ChR2-expressing control group was exposed to the same context without shock. On day 2, all mice were placed in a different context, in which the ChR2-expressing fear-conditioned group ($n = 8$) showed significant fear behaviour (freezing) only during light stimulation, compared with unconditioned ChR2 (no shock, $n = 6$) or shocked control groups (eYFP, $n = 6$, $P < 0.001$, two-way analysis of variance (ANOVA) with repeated measures; Extended Data Fig. 2b). The time to freezing and time to unfreezing with light on/off switching were largely consistent across animals. On day 3, mice were placed back in the original context, verifying in both ChR2 and eYFP fear-conditioned cohorts strong memory encoding and retrieval, with significantly greater levels of freezing compared with no-shock controls (Extended Data Fig. 2c; $P < 0.001$, unpaired *t*-test).

This observation that cells contributing to the AC-CA projection can activate contextually conditioned fear behaviour was replicated and extended using a complementary anterograde projection-targeting strategy. We injected AAVdj-ChR2-eYFP (or AAVdj-eYFP

in a parallel cohort) into the AC, and targeted light stimulation to terminals in the hippocampus (Fig. 2a). We again observed significant freezing to optical stimulation in the neutral context only in the ChR2 group (Supplementary Video 1) compared with the no-shock and eYFP controls (Fig. 2b; $n = 8$ for all groups; $P < 0.001$, two-way ANOVA with repeated measures). These animals exhibited the same characteristic latency to freezing during light stimulation as in the previous experiment. We next tested whether this consistent behavioural response was indeed due to reactivation of a fear memory, rather than due to direct nonspecific drive of fear behaviour. The same mice corresponding to those shown in Fig. 2a, b were subjected to several days of contingency degradation by exposure to context A without shock (Methods), after which stimulation with light failed to produce significant freezing in ChR2 animals, as with no-shock and eYFP controls (Fig. 2c and Supplementary Video 2). Fear conditioning was then reinstated in these mice in a new context, after which light stimulation once again reliably produced freezing in ChR2 mice compared with no-shock and eYFP controls (Fig. 2d; $n = 8$ for all groups; $P < 0.001$, two-way ANOVA with repeated measures; Supplementary Video 3). Preservation of contextual fear memory on day 3 and successful fear memory extinction on day 14 were confirmed (Fig. 2e). While these data demonstrated that cells contributing to the AC-CA projection can drive fear memory recall, it remained possible that any drive of the hippocampus could induce retrieval of a recent strongly represented memory in the hippocampus. However, we found no evidence for this possibility

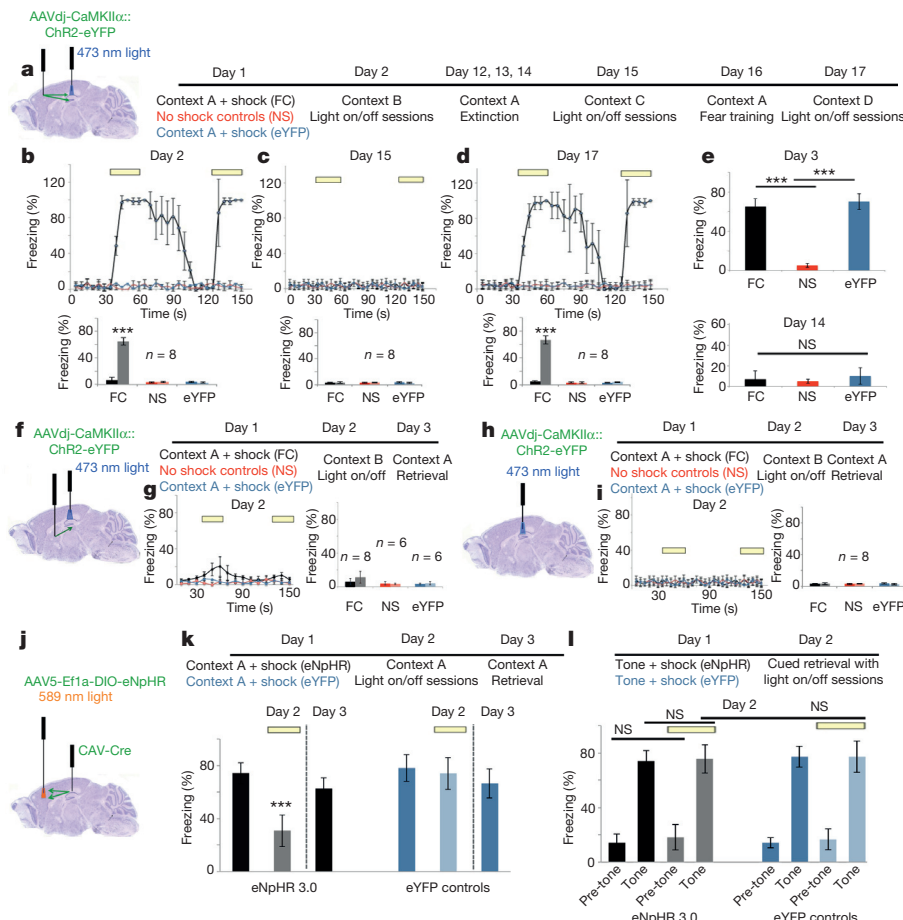


Figure 2 | AC-CA projections control top-down memory retrieval.

a, AAVdj-CaMKII α ::ChR2-eYFP (or eYFP alone) was injected into the AC, and light was targeted to the dorsal hippocampus 5 weeks after injection. Timelines are indicated. FC, fear context; NS, no shock. **b-d**, Percentage time freezing on days 2, 15 and 17: 5 s time bins ($n = 8$; $P < 0.001$, two-way ANOVA with repeated measures) are shown. Throughout this figure, error bars represent standard deviation (s.d.), to facilitate comparison with previously published literature; however, since freezing behaviour is not unbounded, these error bars may overestimate the upper limit of error. Summary bar graphs below are mean \pm s.d. 20 s before light (dark bar) versus 20 s after light (lighter bar). **e**, Preservation of contextual memory (day 3) and contextual extinction (day 14), original context A (mean \pm s.d., $n = 8$, $P < 0.001$, paired t -test). **f**, AAVdj-CaMKII α ::ChR2-eYFP (or eYFP alone) was injected into the medial septum, and light stimulation was targeted to the dorsal hippocampus 5 weeks after injection. **g**, Percentage time freezing during

day 2: 10 s time bins. Right, summary bar graph (not significant, unpaired t -test). **h**, AAVdj-CaMKII α ::ChR2-eYFP (or eYFP alone) injection and light targeting to the dorsal hippocampus 5 weeks after injection. **i**, Percentage time freezing during day 2, 5 s time bins. Right, summary bar graph ($n = 8$; not significant, paired t -test). **j**, CAV-Cre was injected into the dorsal hippocampus, and a Cre-sensitive double-floxed inverted orientation (DIO)-eNpHR3.0 (or DIO-eYFP) was injected into the AC, and light was delivered above the cell bodies in the AC 8 weeks after injection. **k**, Percentage time freezing in context A, day 2 before light (dark bar) versus after light (lighter bar). This effect is reversible on day 3 (to the right of the dotted line). eNpHR3.0: $n = 12$; eYFP: $n = 8$; $P < 0.001$, two-way ANOVA with repeated measures. **l**, Cued conditioning on day 1 followed by retrieval to the tone on day 2 during light on/off sessions. NS, not significant. All data are presented as mean \pm s.d. * $P < 0.05$, ** $P < 0.01$, *** $P < 0.001$.

with two additional control experiments, either directly driving a different (septo-hippocampal) projection (Fig. 2f, g) or directly driving the hippocampus itself (Fig. 2h, i). Preservation of normal contextual fear memory in these mice was confirmed as before (Extended Data Fig. 2d, e; $n = 8$, $P < 0.001$, paired t -test).

These experiments demonstrated that activating AC-CA projecting cells was sufficient to induce contextual memory retrieval; we next tested necessity by targeting the inhibitory opsin eNpHR3.0 to cells giving rise to the projection (Extended Data Fig. 2f, g), with light targeted focally and bilaterally to AC-CA cell bodies (Fig. 2j). We observed striking deficits in both the latency (Extended Data Fig. 2h) and the strength (Fig. 2k; $n = 12$ for eNpHR3.0 group, $n = 8$ for eYFP group, $P < 0.001$, two-way ANOVA with repeated measures) of the fear response in the eNpHR3.0 group (Supplementary Video 4) compared with eYFP controls (Supplementary Video 5). This effect was fully reversible (Fig. 2k). We also found that eNpHR3.0 mice demonstrated intact auditory cued memory recall (Fig. 2l; $n = 8$ for all groups, not significant with paired t -tests), confirming that the loss-

of-function experiments described earlier represented a hippocampus-specific effect of the AC-CA projecting cells.

Taken together, these anatomical, electrophysiological and behavioural data reveal the existence of a previously uncharacterized monosynaptic PFC-to-hippocampus projection. When this circuit is inhibited, fear-conditioned mice are unable to retrieve the fear memory with the same strength or speed as control counterparts, indicating endogenous importance for memory retrieval. In contrast, activation of this circuit is sufficient for robust fear memory retrieval in recently conditioned mice, but not in naive unconditioned mice, mice in which the memory has been extinguished, mice not expressing opsin, or mice receiving other types of direct or indirect drive of hippocampus.

Highly correlated neurons emerge during learning

To observe real-time influences of the AC-CA projection on hippocampal network activity, we adapted the fear-conditioning paradigm to head-fixed mice navigating in a virtual environment on an axially

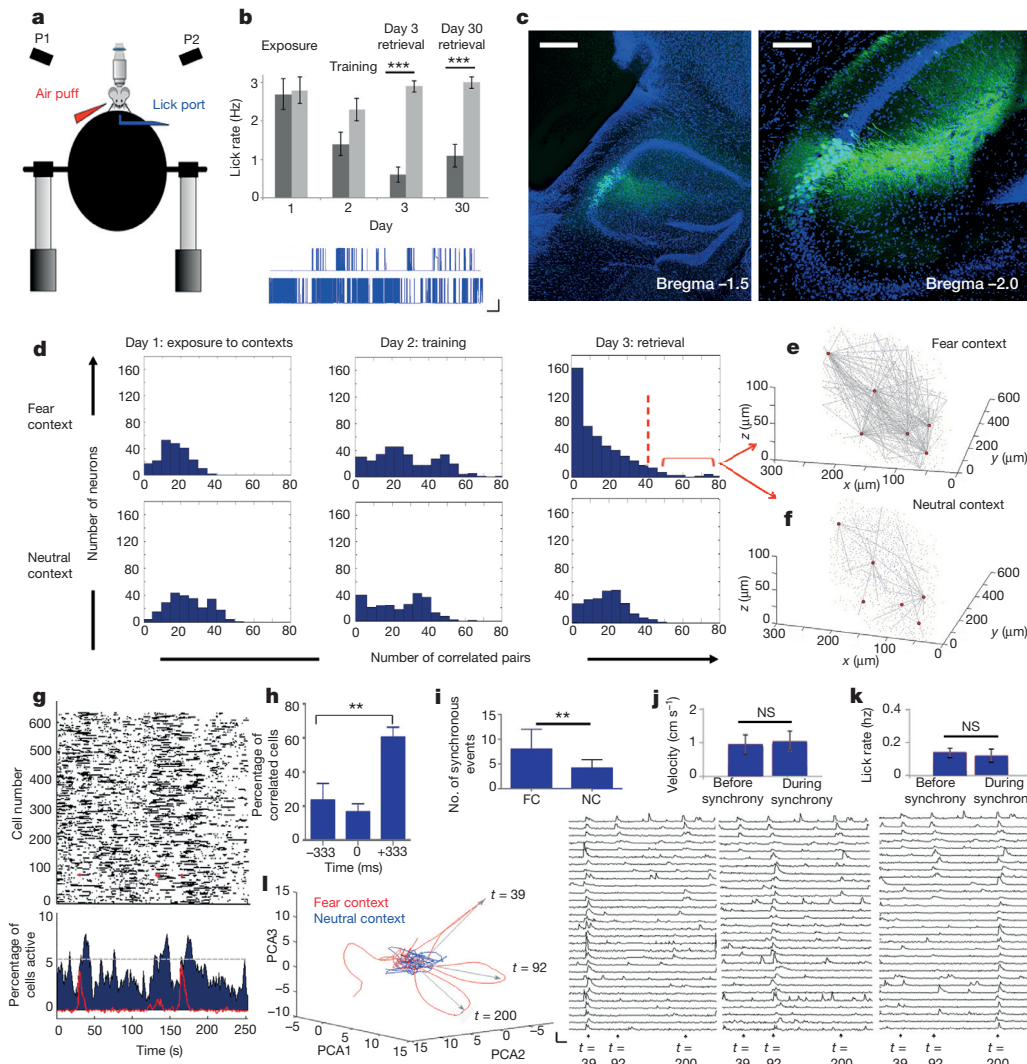


Figure 3 | Memory formation generates highly correlated HC neurons that represent context. **a**, Head-fixed virtual reality setup. Fear was quantified by lick suppression (Methods). P1, projector 1; P2, projector 2. **b**, Lick rates in fear (black) versus neutral (grey) contexts (mean \pm s.d.; $n = 12$; $P < 0.001$, paired t -test). Sample day 3 raw lick profiles in the fear (top) versus neutral (bottom) context. Scale: 1 V, 20 s. **c**, Histology performed 4 weeks after injection/surgical implantation showing implant above GCaMP6m-expressing neurons. Left: $\times 10$; scale bar, 200 μ m. Right: $\times 20$; scale bar, 50 μ m. **d**, Histograms showing number of correlated partners for each neuron in the fear versus neutral contexts for a representative mouse (see Extended Data Fig. 5). **e**, **f**, HC neurons in the fear context (red) (e) have few correlated partners in the neutral context (f). $n = 4$ mice (60 ± 18.2 (s.d.) in the fear context versus 18 ± 15.8 in the neutral context; $P < 0.01$, paired t -test; see Extended Data Fig. 6). **g**, Raster plot (top) and collapsed activity histogram (bottom) during

fixed track ball under a two-photon microscope²⁴. We used lick suppression, rather than immobility, as a measure of fear behaviour in water-restricted mice^{25–27} (Fig. 3a and Methods); mice learned this task and displayed significant lick suppression during retrieval in the fear context, indicating successful memory retrieval (Fig. 3b; $n = 12$, $P < 0.01$, paired t -test). For imaging during behaviour, mice were injected with the genetically encoded Ca^{2+} indicator GCaMP6m²⁸, implanted with a cranial window above CA2/CA3 (Fig. 3c; confirmation of normal hippocampal physiology and behaviour in these mice is shown in Extended Data Fig. 3), and imaged daily in both contexts during training and retrieval (Extended Data Fig. 4a). We targeted imaging preferentially to CA3 neurons by both stereotactic positioning of the imaging field of view (FOV) (Fig. 3c), and by verifying that visualized neurons displayed dendritic processes traveling in the

memory retrieval in one mouse; representative HC neuron time series is overlaid (red). **h**, HC neuron activity onset (time 0) compared with onset activity of their correlated pairs ($n = 67$ HC neurons, $60.3 \pm 6\%$ leading versus $23.2 \pm 10\%$ lagging; $P < 0.01$, unpaired t -test). **i–k**, Synchronous activity (Methods) was quantified ($n = 5$, 8.1 ± 4 events in the fear versus 4.2 ± 1.6 in the neutral context; $P < 0.01$, paired t -test) (**i**), and was not accompanied by significant changes in velocity (**j**) or lick rate (**k**) ($n = 5$ mice; not significant (NS), paired t -test). FC, fear context; NC, neutral context. **l**, Principal component analysis (PCA) from a representative mouse (Extended Data Fig. 9 for additional data sets). Population trajectory in the fear (red) versus the neutral context (blue) was projected onto the respective first three principal components. Right: $\Delta F/F$ traces of HC neurons and their correlated neurons participating in each deflection. **F**, fluorescence; Scale: 400% $\Delta F/F$, 20 s. All error bars represent s.d. * $P < 0.05$, ** $P < 0.01$, *** $P < 0.001$.

focal plane of this dorsal view (Supplementary Video 6; in contrast, CA2 or CA1 neurons show processes traveling out of the focal plane due to the curvature of the pyramidal layer); however, some CA2 neurons are likely to be included. In all cases, fast volumetric ($500 \times 500 \mu\text{m}$ x/y , $100 \mu\text{m}$ z) two-photon imaging was performed, providing access to >400 neurons (Extended Data Fig. 4b).

We first sought to identify features of the functional network that differed consistently across days or contexts. Many features were indistinguishable, including mean response magnitude of active neurons, mean activity event rate, mean activity event duration, and spatial distribution of active neurons (Extended Data Figs 4c–f and 5a). However, we noted a significant increase in the number of neurons active during memory retrieval in the fear context (Extended Data Fig. 5b; $n = 5$ mice); interestingly, this was accompanied by

a significant decrease in mean correlated activity. Although prior studies reported increased correlated activity after learning^{29–31}, a parsimonious unifying explanation could be that reduced mean correlated network activity reflects a state of greater sparsity after learning, in which few neurons engage in considerably higher correlated activity while most become de-correlated. Indeed, binning the number of correlated partners for each neuron revealed a significant distribution shift (Fig. 3d and Extended Data Fig. 5d), from randomly organized Poisson-like correlation distributions before learning to more ordered, power-law-like distributions after learning, with the emergence of a small population of neurons displaying highly correlated activity in the network (HC neurons). Importantly, these network properties were specific to the learned context, and indeed, at the single-neuron level, the highest levels of cell-by-cell correlation were seen in the fear context compared to the neutral context (Fig. 3d and Extended Data Fig. 5d; $n = 5$; $P < 0.01$, paired t -test). Additional quantitative properties were assessed for differential representation of the fear and neutral contexts (Extended Data Fig. 5d–i), revealing that the power-law exponent b provided the largest contribution to this context separation (Extended Data Fig. 5c; $n = 5$, $P < 0.01$), consistent with the emergence of HC neurons representing aspects of fear memory retrieval. Intriguingly, HC neurons in the fear context (Fig. 3e, shown in red) tended to be neurons that had a low degree of correlated partners in the neutral context (Fig. 3f and Extended Data Fig. 6), suggesting that the emergence of HC neurons after learning does not stem simply from strengthening of pre-existing correlated cell assemblies.

To understand better the importance of these HC neurons, we next focused analysis on the activity of the entire network at times when the HC neurons were active. The HC neurons tended to lead rather than lag their correlated pairs (Fig. 3h), which were spatially distributed

throughout the volume (Extended Data Fig. 7a, b). Furthermore, although overall cell-by-cell correlated activity was reduced during the fear retrieval test, significantly more population-wide synchronous events (Fig. 3g, i), which were confirmed to be not related to motion (Fig. 3j, k) and consisted of essentially orthogonal groups of neurons (Fig. 3l and Extended Data Fig. 9), occurred in the fear context; HC neurons were found to lead these broad synchronous events (Extended Data Fig. 7c; $P < 0.001$, Kolmogorov-Smirnov two-tail test), with 78% of HC neurons active within the first 20% of a synchronous event. This event-leading nature could be consistent with a role for HC neurons in recruiting network activity.

Importantly, these analyses were designed to limit the effects of potential confounds of slow fluctuations in the signal (for example, GCaMP6m and Ca^{2+} kinetics) on correlations between neurons (see Methods). Additionally, a fast non-negative deconvolution analysis³² (detailed fully in Methods), for detecting onset of activity while removing slow decay kinetics, yielded consistent results as described earlier for the increased pair-wise correlations in the fear versus neutral context, the event-leading nature of HC neurons compared with their correlated pairs, and the increased synchronous events observed in the fear versus neutral context (Extended Data Fig. 8).

AC-CA projections target HC neurons during retrieval

These volumetric imaging studies during memory retrieval demonstrate the emergence of a sparse set of HC neurons characterized by high correlations and leading of local synchronous events. Such neurons could serve as efficient points of access if preferentially recruited by top-down projections during memory retrieval. To test this idea, we sought to stimulate AC-CA projections while simultaneously imaging the postsynaptic hippocampal network to observe local dynamics directly. Current *in vivo*-tested red-shifted

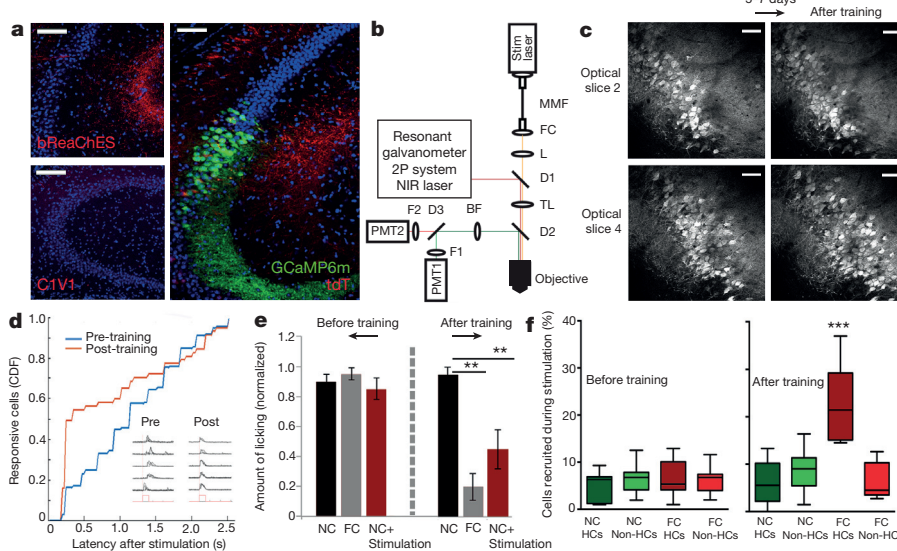


Figure 4 | The AC-CA projection preferentially recruits HC neurons during memory retrieval. **a**, Left, AAV8-CaMKII::bReaChES-eYFP or AAV8-CaMKII::C1V1_{T/T}-eYFP (C1V1_{T/T} denotes the red-light-activated channelrhodopsin engineered and characterized in refs 33 and 47) was injected into the AC, and fibre terminals were visualized in CA3 (red). Scale bars, 60 μm ($\times 20$). Right, AAV8-CaMKII::tdT in the AC, and AAVdj-CaMKII::GCaMP6m in CA2/CA3. Histology 8 weeks after cannula implantation showing preservation of AC-CA projections (red) near GCaMP6m-expressing neurons (green). Scale bar, 50 μm ($\times 20$). **b**, Two-photon imaging and full-field optogenetic stimulation setup (Methods). Green indicates GCaMP6m signals; red, stimulation artefact. D1, 680 nm short-pass dichroic; D2, 594 band/NIR long-pass dichroic; D3, 555 nm long-pass dichroic; FC, fibre couple; F1, 520 \pm 22 nm filter; F2, 624 \pm 20 nm filter; L, 25 mm planoconvex lens; MMF, multimode fibre; NIR BF, near infrared blocking filter; PMT1 and PMT2, GaAsP PMTs; TL, tube lens.

c, Z-projection images (mean over time) at two depths (40 μm apart) from a representative mouse before and after training. Scale bars, 60 μm . **d**, Proportion of cells responding (CDF, cumulative distribution function) to AC-CA stimulation as a function of latency ($n = 4$ mice; 12 trials, $P = 0.002$; Kolmogorov-Smirnov two-tail test, $\kappa = 0.2673$). Sample traces in inset (red box: stimulation duration). Consecutive trials are overlaid. **e**, Optical stimulation in the neutral context induces significant lick suppression after training ($n = 4$ mice, 12 total trials, mean \pm s.d., $P < 0.01$, paired t -test). No lick suppression was seen before training (not significant, paired t -test). FC, fear context; NC, neutral context. **f**, Fraction of fear- and neutral-context HC and non-HC neurons recruited during before- ($n = 3$ mice, 10 total trial) and after-training optical stimulation ($n = 4$ mice, 12 total trials, $P < 0.001$, one-way ANOVA); mean, quartile, minimum and maximum are shown. ** $P < 0.01$, *** $P < 0.001$.

opsins, however, were not suitable because, as we and others have found, C1V1 (ref. 33) does not traffic well to the terminals of long-range projections, and ReaChR³⁴ (despite adequate trafficking) shows lower photocurrents and reduced spike fidelity in mammals. By extensively modifying ReaChR to include ChETA-based³⁵ and other mutations, we generated a red-shifted opsin termed bReaChES with strong photocurrents, high spike fidelity (Extended Data Fig. 10) and robust trafficking in long-range projections (Fig. 4a).

Mice were injected with GCaMP6m in CA3 and bReaChES in the AC, and implanted with a cannula above CA2/CA3 (Fig. 4a) for simultaneous one-photon stimulation of projection terminals and two-photon imaging of CA2/CA3 pyramidal neurons through the same window (Fig. 4b). To test the causal effect of the projection, we performed multiple optical-stimulation trials both before and after fear conditioning, while tracking the same neurons across contexts and days (Fig. 4c). While trial-to-trial variability existed in the number and identity of neurons activated, fear conditioning was found consistently to increase the fraction of cells that were time locked to the onset of optogenetic stimulus of the top-down projection (Fig. 4d; $P = 0.002$, Kolmogorov–Smirnov two-tail test). Finally, we directly tested recruitment of the memory-associated HC neurons by this projection. To do this, we first established that, consistent with earlier results, head-fixed mice were able to learn the contextual fear conditioning task and that stimulation of the AC–CA projection induced fear memory retrieval only after training and not before (Fig. 4e). Quantification over many trials indicated that stimulation of the AC–CA projection recruited relatively few (~5%) HC neurons in either the fear or neutral context before training, whereas there was a marked increase (~20%) in the fraction of HC neurons recruited after training; recruitment of non-HC neurons in the fear context, and recruitment of any neurons in the neutral context, remained unchanged and low (Fig. 4f). These results further demonstrated swift reorganization of the functional impact of the AC–CA projection, with preferential recruitment of HC neurons associated with the recently formed contextual fear memory. Together, these findings reveal a means by which top-down circuit influences could organize and engage with salient memory representations to enable efficient retrieval.

Discussion

We have identified a direct projection from the AC to the hippocampus with properties that mediate retrieval of recently encoded memory traces. The ability of the AC to select appropriate targets among hippocampal pyramidal neurons during context retrieval points to potential reciprocity between these two regions; the hippocampus is well positioned to inform the AC regarding context through bottom-up pathways, after which the AC can access and mobilize engrams in the hippocampus for top-down control of retrieval. The AC may also form an independent representation during training, as suggested by the speed (within 1 day post-training) with which the AC–CA projection can mediate top-down retrieval. This rapid retrieval also demonstrates that the AC is engaged early during the memory encoding process, as has been suggested^{9–11}, which, together with the previous finding of hippocampal engagement even at later time points³⁶, suggests a shift towards viewing the AC and hippocampus, and their bidirectional communication, as having shared involvement in both early and late stages of memory. The speed and specificity of the top-down retrieval also underscores likely plasticity at the AC–CA terminals for dynamic access to recently allocated neurons in the hippocampus.

We have found that this top-down control over contextual memory involves preferential recruitment of a sparse set of hippocampal neurons that are highly correlated in the local network and that tend to lead population-wide synchronous events, but only in the memory context and in a manner only seen after training. Sparsification of memory-associated networks during learning has been observed^{30,37–40}

and computationally predicted^{20,41,42}, since hierarchical networks with few extensively connected hub-like nodes, as observed here, are well suited for memory stability (random degradation of the network will probably affect non-hub nodes that are less consequential to the memory representation). But beyond memory stability, the emergence of contextual memory-specific HC neurons could facilitate efficient access to engrams, in a process suitable for memories that are strongly encoded via repetition, reward, or emotional saliency. This circuit property could be broadly relevant, helping to explain how even single cortical neurons can in some cases drive network activity and behaviour^{43–46}.

In the future, improvements in two-photon stimulation of individually targeted neurons over large three-dimensional volumes, together with simultaneous recording of network activity^{47–49}, may enable further delineation of the causal role of HC neurons during memory retrieval. Also of importance is the exploration of the molecular and structural properties of the observed HC neurons, and their inputs and outputs, through high-content methods such as single-cell RNA-sequencing and CLARITY (a method for creating labelled hybrids or composites of biomolecules in tissue covalently linked to acrylamide-related polymer hydrogels, which allows removal of unlinked tissue elements to create transparency and high-resolution accessibility to the macromolecular labels)⁵⁰. More broadly, further study of the AC–CA and other top-down projections with the circuit tracing and control methods described here may help to elucidate brain-wide regulation of memory in normal behaviour and in maladaptive states involving aberrant communication between PFC and hippocampus.

Online Content Methods, along with any additional Extended Data display items and Source Data, are available in the online version of the paper; references unique to these sections appear only in the online paper.

Received 27 May; accepted 10 August 2015.

Published online 5 October 2015.

- Kandel, E. R., Dudai, Y. & Mayford, M. R. The molecular and systems biology of memory. *Cell* **157**, 163–186 (2014).
- Han, J. H. et al. Neuronal competition and selection during memory formation. *Science* **316**, 457–460 (2007).
- Han, J. H. et al. Selective erasure of a fear memory. *Science* **323**, 1492–1496 (2009).
- Yiu, A. P. et al. Neurons are recruited to a memory trace based on relative neuronal excitability immediately before training. *Neuron* **83**, 722–735 (2014).
- Reijmers, L. G., Perkins, B. L., Matsuo, N. & Mayford, M. Localization of a stable neural correlate of associative memory. *Science* **317**, 1230–1233 (2007).
- Liu, X. et al. Optogenetic stimulation of a hippocampal engram activates fear memory recall. *Nature* **484**, 381–385 (2012).
- Garner, A. R. et al. Generation of a synthetic memory trace. *Science* **335**, 1513–1516 (2012).
- Ramirez, S. et al. Creating a false memory in the hippocampus. *Science* **341**, 387–391 (2013).
- Tse, D. et al. Schema-dependent gene activation and memory encoding in neocortex. *Science* **333**, 891–895 (2011).
- Lesburguères, E. et al. Early tagging of cortical networks is required for the formation of enduring associative memory. *Science* **331**, 924–928 (2011).
- Bero, A. W. et al. Early remodeling of the neocortex upon episodic memory encoding. *Proc. Natl. Acad. Sci. USA* **111**, 11852–11857 (2014).
- Frankland, P. W. & Bontempi, B. The organization of recent and remote memories. *Nature Rev. Neurosci.* **6**, 119–130 (2005).
- Ressler, K. J. & Mayberg, H. S. Targeting abnormal neural circuits in mood and anxiety disorders: from the laboratory to the clinic. *Nature Neurosci.* **10**, 1116–1124 (2007).
- Taylor, S. F. et al. Meta-analysis of functional neuroimaging studies of emotion perception and experience in schizophrenia. *Biol. Psychiatry* **71**, 136–145 (2012).
- Wilson, S. J., Sayette, M. A. & Fiez, J. A. Prefrontal responses to drug cues: a neurocognitive analysis. *Nature Neurosci.* **7**, 211–214 (2004).
- Nadel, L. & Moscovitch, M. Memory consolidation, retrograde amnesia and the hippocampal complex. *Curr. Opin. Neurobiol.* **7**, 217–227 (1997).
- Winocur, G., Moscovitch, M. & Bontempi, B. Memory formation and long-term retention in humans and animals: convergence towards a transformation account of hippocampal-neocortical interactions. *Neuropsychologia* **48**, 2339–2356 (2010).
- Strogatz, S. H. Exploring complex networks. *Nature* **410**, 268–276 (2001).
- Barabási, A. L. & Oltvai, Z. N. Network biology: understanding the cell's functional organization. *Nature Rev. Genet.* **5**, 101–113 (2004).

20. Bullmore, E. & Sporns, O. Complex brain networks: graph theoretical analysis of structural and functional systems. *Nature Rev. Neurosci.* **10**, 186–198 (2009).
21. Hermundstad, A. M., Brown, K. S., Bassett, D. S. & Carlson, J. M. Learning, memory, and the role of neural network architecture. *PLOS Comput. Biol.* **7**, e1002063 (2011).
22. Wickersham, I. R., Finke, S., Conzelmann, K. K. & Callaway, E. M. Retrograde neuronal tracing with a deletion-mutant rabies virus. *Nature Methods* **4**, 47–49 (2007).
23. Soudais, C., Laplace-Builhe, C., Kiss, K. & Kremer, E. J. Preferential transduction of neurons by canine adenovirus vectors and their efficient retrograde transport *in vivo*. *FASEB J.* **15**, 2283–2285 (2001).
24. Dombeck, D. A., Harvey, C. D., Tian, L., Looger, L. L. & Tank, D. W. Functional imaging of hippocampal place cells at cellular resolution during virtual navigation. *Nature Neurosci.* **13**, 1433–1440 (2010).
25. Mahoney, W. J. & Ayres, J. J. B. One-trial simultaneous and backward fear conditioning as reflected in conditioned suppression of licking in rats. *Anim. Learn. Behav.* **4**, 357–362 (1976).
26. Bouton, M. E. & Bolles, R. C. Conditioned fear assessed by freezing and by the suppression of three different baselines. *Anim. Learn. Behav.* **8**, 429–434 (1980).
27. Lovett-Barron, M. et al. Dendritic inhibition in the hippocampus supports fear learning. *Science* **343**, 857–863 (2014).
28. Chen, T. W. et al. Ultrasensitive fluorescent proteins for imaging neuronal activity. *Nature* **499**, 295–300 (2013).
29. Cheng, S. & Frank, L. M. New experiences enhance coordinated neural activity in the hippocampus. *Neuron* **57**, 303–313 (2008).
30. Komiyama, T. et al. Learning-related fine-scale specificity imaged in motor cortex circuits of behaving mice. *Nature* **464**, 1182–1186 (2010).
31. Modi, M. N., Dhawale, A. K. & Bhalla, U. S. CA1 cell activity sequences emerge after reorganization of network correlation structure during associative learning. *eLife* **3**, e01982 (2014).
32. Vogelstein, J. T. et al. Fast nonnegative deconvolution for spike train inference from population calcium imaging. *J. Neurophysiol.* **104**, 3691–3704 (2010).
33. Yizhar, O. et al. Neocortical excitation/inhibition balance in information processing and social dysfunction. *Nature* **477**, 171–178 (2011).
34. Lin, J. Y., Knutson, P. M., Muller, A., Kleinfeld, D. & Tsien, R. Y. ReaChR: a red-shifted variant of channelrhodopsin enables deep transcranial optogenetic excitation. *Nature Neurosci.* **16**, 1499–1508 (2013).
35. Gunaydin, L. A. et al. Ultrafast optogenetic control. *Nature Neurosci.* **13**, 387–392 (2010).
36. Goshen, I. et al. Dynamics of retrieval strategies for remote memories. *Cell* **147**, 678–689 (2011).
37. Vinje, W. E. & Gallant, J. L. Sparse coding and decorrelation in primary visual cortex during natural vision. *Science* **287**, 1273–1276 (2000).
38. Olshausen, B. A. & Field, D. J. Sparse coding of sensory inputs. *Curr. Opin. Neurobiol.* **14**, 481–487 (2004).
39. Yassin, L. et al. An embedded subnetwork of highly active neurons in the neocortex. *Neuron* **68**, 1043–1050 (2010).
40. Gdalyahu, A. et al. Associative fear learning enhances sparse network coding in primary sensory cortex. *Neuron* **75**, 121–132 (2012).
41. Buzsáki, G., Geisler, C., Henze, D. A. & Wang, X.-J. Interneuron Diversity series: circuit complexity and axon wiring economy of cortical interneurons. *Trends Neurosci.* **27**, 186–193 (2004).
42. Perin, R., Berger, T. K. & Markram, H. A synaptic organizing principle for cortical neuronal groups. *Proc. Natl Acad. Sci. USA* **108**, 5419–5424 (2011).
43. Bonifazi, P. et al. GABAergic hub neurons orchestrate synchrony in developing hippocampal networks. *Science* **326**, 1419–1424 (2009).
44. Brecht, M., Schneider, M., Sakmann, B. & Margrie, T. W. Whisker movements evoked by stimulation of single pyramidal cells in rat motor cortex. *Nature* **427**, 704–710 (2004).
45. Houweling, A. R. & Brecht, M. Behavioural report of single neuron stimulation in somatosensory cortex. *Nature* **451**, 65–68 (2008).
46. Li, C. Y., Poo, M.-M. & Dan, Y. Burst spiking of a single cortical neuron modifies global brain state. *Science* **324**, 643–646 (2009).
47. Prakash, R. et al. Two-photon optogenetic toolbox for fast inhibition, excitation and bistable modulation. *Nature Methods* **9**, 1171–1179 (2012).
48. Rickgauer, J. P., Deisseroth, K. & Tank, D. W. Simultaneous cellular-resolution optical perturbation and imaging of place cell firing fields. *Nature Neurosci.* **17**, 1816–1824 (2014).
49. Packer, A. M., Russell, L. E., Dalgleish, H. W. & Häusser, M. Simultaneous all-optical manipulation and recording of neural circuit activity with cellular resolution *in vivo*. *Nature Methods* **12**, 140–146 (2015).
50. Chung, K. et al. Structural and molecular interrogation of intact biological systems. *Nature* **497**, 332–337 (2013).

Supplementary Information is available in the online version of the paper.

Acknowledgements We thank B. K. Lim for the rabies virus and S. Pak for assistance with histology. We thank the entire Deisseroth laboratory for thoughtful comments, with particular gratitude to M. Lovett-Baron, A. Andelman and W. Allen for their helpful discussions throughout. K.D. is supported by the Defense Advanced Research Projects Agency Neuro-FAST program, National Institute of Mental Health, National Institute on Drug Abuse, National Science Foundation, the Simons Foundation, the Tarlton Foundation, the Wiegers Family Fund, the Nancy and James Grosfeld Foundation, the H.L. Snyder Medical Foundation, and the Samuel and Betsy Reeves Fund. This work is supported by an Ellison Life Sciences Research Foundation (LSRF) fellowship (P.R.), a Simons LSRF fellowship (J.H.M.), the German Academic Exchange Service DAAD (A.B.) and the Fidelity Foundation (S.Y.L.). All tools and methods are distributed and supported freely (<http://www.optogenetics.org>).

Author Contributions P.R. and K.D. designed the experiments. P.R. performed anatomical tracing, optogenetic behaviour, virtual reality behaviour, hippocampal cranial window surgeries and *in vivo* imaging experiments, and collected all associated data. S.S. wrote custom code to extract neural sources and performed computational analysis on all of the *in vivo* calcium imaging datasets. P.R. and J.H.M. collected data from simultaneous one-photon stimulation and two-photon imaging experiments, and J.H.M. and S.S. analysed those data. E.F. and S.Y.L. performed patch electrophysiology experiments. C.K.K. designed the virtual reality infrastructure. S.Y.L., A.B. and C.R. designed and tested the bReaChES opsin. A.J. performed injections and fibre implant surgeries. M.L. assisted with behaviour. C.L. assisted with cranial window surgeries and statistical analysis. P.R. and K.D. wrote the paper; K.D. supervised all aspects of the work. All authors discussed findings, edited and contributed to the final version of the manuscript.

Author Information Reprints and permissions information is available at www.nature.com/reprints. The authors declare no competing financial interests. Readers are welcome to comment on the online version of the paper. Correspondence and requests for materials should be addressed to K.D. (deissero@stanford.edu).

METHODS

Animals. Wild-type C57Bl6/J male mice were group housed three to five to a cage and kept on a reverse 12 h light/dark cycle with *ad libitum* food and water (except in virtual reality behaviour experiments, for which water was restricted; details later). Experimental protocols were approved by Stanford University Institutional Animal Care and Use Committee (IACUC) and meet the guidelines of the National Institutes of Health guide for the Care and Use of Laboratory Animals. The target number of subjects used in each experiment was determined based on numbers reported in published studies. No statistical methods were used to predetermine sample size.

Anatomical tracing and histology. Viral injections were carried out under protocols approved by Stanford University IACUC and were performed in mice anaesthetized with 1–2% isoflurane using a stereotaxic apparatus (Kopf Instruments). For retrograde tracing, 4–5-week-old wild-type male mice were injected slowly (50 nl min^{-1}) with small amounts (200 nl) of highly concentrated glycoprotein-deleted rabies virus tagged with tdTomato (RV-tdTomato)²² in the dorsal hippocampus (A/P: −1.5 mm; M/L: +1.75 mm; D/V: −1.8 mm) with a 1 μl Hamilton syringe and a 35-gauge bevelled needle (World Precision Instruments) under the control of a UMP3 syringe pump (WPI). Following injections, the incisions were closed using Vettbond tissue adhesive (Fischer), and mice were allowed to recover and were housed for 5 days to allow for expression before their brains were collected for histological analysis. In the case of anterograde tracing, 4–5-week-old wild-type male mice were injected (150 nl min^{-1}) with 500 nl of AAV5-CaMKII α ::eYFP (titre: $2 \times 10^{12} \text{ vg ml}^{-1}$) in dorsal anterior cingulate (A/P: +1; M/L: −0.35; D/V: +1.2) and were housed for 30 days to allow for expression in terminals before collection of brains for histological analysis.

For histological analysis, injected mice were transcardially perfused with ice-cold 1× PBS, immediately followed by perfusion of 4% paraformaldehyde (PFA). Brains were fixed overnight in PFA, then transferred to a 30% sucrose/PBS solution. Coronal sections of either 40 μm (for retrograde tracing with RV) prepared using a freezing microtome (Leica) or 300 μm (for anterograde tracing with AAV5) prepared using a vibratome (Leica) were collected and stored in a cryoprotectant solution (25% glycerol, 30% ethylene glycol, in PBS) until further processing. For DAPI staining, slices were washed in PBS, incubated for 20 min with DAPI at 1:50,000, washed again in PBS, then mounted with PVA-DABCO (Sigma). A scanning confocal microscope (TCS SP5, Leica) and LAS AF software (Leica) was used to obtain and analyse images.

Acute slice electrophysiology of AC-CA synapses. Acute brain slices were prepared from mice 6–8 weeks following viral injection with AAV5-CaMKII α ::ChR2(H134R)-eYFP, to allow sufficient time for channelrhodopsin to express in axon terminals. After lethal anaesthesia, mice were transcardially perfused with cold sucrose slicing solution (see later) before decapitation, following which the brain was rapidly extracted and submerged in ice-cold sucrose-based slicing solution (234 mM sucrose, 26 mM NaHCO₃, 11 mM glucose, 10 mM MgSO₄·7H₂O, 2.5 mM KCl, 1.25 mM Na₂PO₄·H₂O, 0.5 mM CaCl₂·2H₂O). Coronal hippocampal slices (300 μm thick) were cut on a Leica vibratome (Leica VT1000S) in sucrose solution and then submerged in a hypertonic recovery solution (artificial cerebrospinal fluid (ACSF) at an 8% increased osmolarity) at 33 °C for 15 min before being transferred to standard ACSF (123 mM NaCl, 26 mM NaHCO₃, 11 mM glucose, 3 mM KCl, 2 mM CaCl₂·2H₂O, 1.25 mM Na₂PO₄·H₂O, 1 mM MgCl₂·6H₂O) for a further 45 min at 33 °C, at which point they were transferred to room temperature.

Whole-cell patch-clamp recordings from CA3/CA1 hippocampal neurons were performed on an upright Leica DM-LFSA microscope. Borosilicate glass (Sutter Instruments) pipette resistances were pulled to 3–6 M Ω and filled with potassium gluconate intracellular solution (130 mM KGluconate, 10 mM KCl, 10 mM HEPES, 10 mM EGTA, 2 mM MgCl₂, pH adjusted with KOH to 7.3). Voltage and current-clamp recordings were performed using pClamp (Axon Instruments). Cells with leak current greater than −200 pA or series resistance greater than 35 M Ω were excluded. Light stimulation was performed using a 300 W DG-4 lamp (Sutter Instruments) with an external filter for blue light (wavelength in nm/bandwidth in nm: 470/20). Light pulses (2–5 ms pulse width) were delivered through a $\times 40$, 0.8 NA water-immersion objective at 4–10 mW mm^{−2} light power density. Latencies were measured as light pulse start to EPSC initiation.

Optogenetics and behaviour. After injection with the indicated virus (for example, CAV or RV, expressing ChR2, eNpHR3.0, or eYFP) at the appropriate location (for example, cingulate, hippocampus, or medial septum), as described in Fig. 2 and Extended Data Figs 2 and 4, 5-week-old wild-type male mice were implanted with implantable fibre-optic lightguides (IFLs) consisting of a 2.5-mm-diameter metal ferrule with 0.22 NA and a 200- μm -thick protruding cleaved bare optic fibre cut to the desired length (Thorlabs) as previously described³⁶, either at the injection site (typically ~0.2 mm dorsal to the injection site) or at the termi-

nals for stimulation experiments as indicated in the figure legends. For inhibition experiments, dual fibre-optic cannulas of 200 μm thickness and 0.22 NA spaced 0.7 mm apart were used to target anterior cingulate bilaterally, and two-ferrule cannulas spaced 3 mm apart were used to target hippocampus bilaterally. Mice were typically allowed to recover and housed for 1 month to allow for adequate expression before behavioural testing. All animals undergoing behavioural experiments were acclimated to a 12 h reverse light/dark cycle, handled for several days, and before behavioural testing, were acclimated to the room in which experiments were to be conducted for at least 30 min.

The fear conditioning apparatus consisted of a square conditioning cage (18 × 18 × 30 cm) with a grid floor wired to a shock generator and a scrambler, surrounded by an acoustic chamber (Coulburn Instruments). The apparatus was modified to enable light delivery during retrieval testing. Contextual fear conditioning was performed by placing mice in the conditioning cage (visual cues: bare walls; tactile cues: grid floor; odour cues: 70% ethanol) for 6 min, while receiving four 2 s shock pulses of 7 mA each at 1 min intervals, with the first shock presented 2 min after placing the mouse in the conditioning context. A fraction of animals of the same cohort were not fear conditioned, and instead served as a control group that were just exposed to the conditioning context for the same amount of time (6 min) but did not receive any associated shocks. The following day, all mice were tested in a different ‘neutral’ cage (visual cues: coloured shapes; tactile cues: smooth paper towel covered plexiglass floor; odour cues: 1% acetic acid) for light-mediated fear retrieval.

For stimulation experiments, optical stimulation through the fibre-optic connector was administered by delivering light through a patch-cord connected to a 473 nm laser in 30 s light-on/1 min light-off sessions. During light-on sessions, stimulation was delivered at 20 Hz, 15 ms pulses, with 8–10 mW power at the fibre tip. On the third day, all mice were then returned to the original conditioning context for 2.5 min to assess intact natural fear memory retrieval. In some cases, subsequent extinction of fear memory was performed by placing mice in the original conditioning chamber for three consecutive days, for 5 min each, without shock. Light-induced fear retrieval was then tested in the neutral context 24 h following the last extinction training session. Subsequent reinstatement was performed by again placing the animals back in the conditioning context for one 6 min interval and providing four 2 s shock pulses of 7 mA each at 1 min intervals. A final light-induced fear retrieval testing was performed 24 h later as described earlier.

For loss of function experiments, optical inhibition through a fibre-optic connector was administered by delivering light through a dual patch-cord connected to a 589 nm laser. Constant light at 8–10 mW was used at the fibre tip to deliver inhibition either at cell bodies or terminals. On the first day, both eNpHR3.0 and eYFP control groups were trained to contextual fear conditioning as described earlier, and on the second day, mice were allowed to perform retrieval as usual during light off for the first 2 min, to assess baseline freezing in each animal. Then light was turned on for the next 30 s (not longer, as the potential for extinction related unfreezing could confound light-related unfreezing at time points succeeding the typical 2–3-min retrieval protocol). Freezing scores during the 30 s light sessions were compared with the per cent freezing during 30 s of the immediately preceding light-off sessions. On the third day, all mice underwent retrieval in the conditioning context for 2 min with light off to test for reversal of light-induced behaviour. After context conditioning and retrieval, all mice subsequently underwent auditory-cued conditioning (cued conditioning was done separately from context conditioning to ensure robust conditioning to both context and cue, since when performed together, mice often develop robust conditioning to tone (the more salient cue) and only weak conditioning to context). To perform auditory-cued fear conditioning, mice were placed in a different context (with coloured shapes as visual cues and a smooth floor), for 6 min, where after the first 2 min, four 20 s auditory cues consisting of 2.9 kHz tone was played at 1 min intervals, each followed by a 2 s 7 mA shock. Retrieval on the subsequent day was performed by presenting the tone four times (two during light off and two during light on) at 1 min intervals and per cent freezing was assessed during the 20 s post-tone compared with the immediately preceding 20 s during tone, for both light-off and light-on conditions. Latency measures were performed as separate experiments, using the same cohorts; after finishing contextual and cued conditioning, these mice were retrained (contextually fear conditioned) to the first conditioning context. On the following day, 2 min retrieval was performed in the conditioning context with light on the entire time to test for latency to freezing, where latency was defined as the first instance in time that the animal was immobile for 5 consecutive seconds. Freezing in all experiments was scored by an experimenter blinded to the treatment group. Randomization of animals to experimental and control groups was performed by an experimenter with no explicit randomization algorithm used. All of the results were analysed by Student’s *t*-test or two-way ANOVA, followed by post-hoc tests, as applicable.

Hippocampal cranial window. C57BL/6J male mice were injected with 500 nl of AAVdj-CaMKIIα::GCaMP6m in CA3 (A/P: -1.7, M/L: +1.9, D/V: -1.9) and allowed to recover for at least 1 week before surgical implantation of a cranial window above CA2/CA3 for optical access similar to previously described hippocampal preps²⁴. Briefly, mice were injected with 80 mg kg⁻¹/6 mg kg⁻¹ of ketamine/xylazine intraperitoneally, and maintained under 1.0–2.0% isoflurane throughout. For optimal window placement to access CA2/CA3, the mouse's head was angled during surgery such that the skull location at the CA2/CA3 injection site was level and exactly perpendicular to dorsal views of the head. A circular titanium headplate (7 mm in diameter) was centred over CA2/CA3 and adhered to the skull with adhesive cement (Metabond; Parkell) and a ~3 mm craniotomy was made in the centre using a trephine (Fisher). Parts of cortical region S1 and of parietal association cortex were vacuum-aspirated, with care taken to avoid the ventricle, until white matter was visible above the hippocampus. Vacuum aspiration was done with a 27-gauge blunt needle while irrigating with chilled 1× PBS. The top layer of white matter above the hippocampus was further removed by vacuum aspiration with a 31-gauge blunt needle, but care was taken to preserve deep layers of external capsule and the alveus (to preserve afferents and efferents to hippocampus). A forceps was used to manually insert a cylindrical borosilicate glass implant until the floor of the implant rested against the hippocampus. The implant was constructed from a 3.0-mm-diameter glass capillary tube (Friedrich & Dimmock) custom cut to 1.5 mm length, adhered on one end to a 3.0 mm diameter coverslip of #0 thickness (Warner Instruments) using UV-curing optical glue (Norland Products). The top of the implant extruding from the craniotomy was then secured to the skull using Metabond adhesive cement. After surgery, mice were given 5 mg kg⁻¹ carprofen subcutaneously and allowed to recover for at least 1 week before behaviour training.

To ensure that the above manipulations (including GCaMP6m virus injection into CA3, GCaMP6m expression, and surgical excavation of certain regions of cortex) did not affect normal physiological properties of the hippocampus, we performed control experiments to assess Ca²⁺-dependent physiology in weakly versus strongly expressing CA3 neurons *in vitro*, spontaneous activity in weakly versus strongly expressing CA3 neurons *in vivo*, and behavioural measurements before and after placement of the cannula (Extended Data Fig. 3).

Virtual reality behaviour. We used a custom built virtual reality environment, modified from previously reported versions^{24,51}. A 200-mm-diameter styrofoam ball (Graham Sweet Studios) was axially fixed with a 6-mm-diameter assembly rod (Thorlabs) passing through the centre of the ball and resting on 90° post holders (Thorlabs) at each end, allowing free forward and backward rotation of the ball. Mice were head-fixed in place above the centre of the ball using a head-plate mount⁵². Virtual environments were designed in game development software Unity3d (<http://www.unity3d.com>). The virtual environment was displayed by back-projection onto projector screen fabric stretched over a clear acrylic hemisphere with a 14-inch diameter placed ~20 cm in front of the centre of the mouse. The screen encompasses ~220° of the mouse's field of view. The virtual environment was back-projected onto this screen using two laser-scanning projectors (Microvision), each projector covering one half of the screen. To create a flat image on the three-dimensional screen, we warped the two-dimensional image of the virtual environment using video manipulation software (Madmapper). The game engine allowed scripts written in JavaScript or C# to trigger external events based on the mouse's interactions with the virtual environment by communicating over a TCP socket to custom Python control software. A LabJackU6 (<http://labjack.com>) was used to time-lock virtual environment events and imaging frame times, to record mouse licking behaviour with incoming TTL pulses from the lickometer (Island Motion), and to send TTL pulses to deliver solenoid-gated water rewards (delivered from a gravity-assisted syringe attached to tubing connected to the lickometer) and aversive air puffs (from a compressed air tank to a tube ending in a pipette tip facing the mouse's snout). Tactile and odour cues were fixed directly to each of two Styrofoam balls representing the two separate contexts. Auditory stimuli were presented through speakers situated behind the animal. The mouse's movements on the ball were recorded using an optical computer mouse (Logitech) that interfaced with the virtual environment software.

For fear conditioning in the virtual environment, mice were water restricted (>80% pre-deprivation weight) and habituated to handling, head-fixation, and the virtual environment for at least 2 weeks, with free access to small water rewards (~0.5 µl per 10 licks) while on the ball. By the end of 2 weeks (one 5-min session per day), mice appeared comfortable and alert on the ball. After habituation, mice underwent a 4-day fear conditioning training and testing protocol. On day 1, mice were exposed to two contexts that differed in visual (blue triangles versus pink vertical stripes), tactile (smooth side of Velcro versus sharp side of Velcro fixed onto running ball), odourant (acetic acid versus ethanol), and auditory cues (8 kHz phasic tone versus 3 kHz pure tone) for 5 min each. On day 2, mice were provided with 8 aversive air puffs to the snout (500 ms, 10 psi) at

randomly timed intervals throughout the 5 min while in the fear context, but not while in the neutral context for 5 min. On days 3 and 30, mice were placed back in each of the two contexts for 5 min for retrieval.

Imaging. Five mice were imaged on all days, in 5-min sessions, during exposure, training, and retrieval. We used a resonant galvanometer two-photon microscope (Prairie Technologies). We used the genetically encoded calcium indicator GCaMP6m in all experiments (GCaMP6m was amplified from Addgene plasmid #40754 by PCR and subcloned into an AAV backbone under the control of the CaMKIIα promoter.) All experiments were performed using a Coherent Ultra II Ti-Sapphire pulsed laser tuned to 920 nm to excite GCaMP6m through a ×20 0.5 LUMPlanFL/N (Olympus) water-immersion objective interfacing with the implanted cannula through a few drops of distilled water. Fluorescence was detected through gallium arsenide phosphide (GaAsP) photomultiplier tubes (PMTs) using the PrairieView acquisition software. High speed *z* stacks were collected in the green channel (using a 520/44 bandpass filter, Semrock) at 512 × 512 pixels covering each *x*-*y* plane of 500 µm × 500 µm over a depth of ~100 µm (3–7 *z* slices ~10–20 µm apart) by coupling the 30 Hz rapid resonant scanning (*x*-*y*) to a *Z*-piezo to achieve ~6 Hz per volume.

Data analysis. Later, we describe the methods to extract cells (pre-processing), obtain cellular-level activity ($\Delta F/F$) measures (processing), and evaluate population-level activity measures (post-processing). In statistical analysis of the post-processed data, both parametric and non-parametric tests were employed as appropriate. In cases where normality could not be assessed (low sample sizes), we ensured that there were no significant outliers (by Grubbs' test) and that the variance between groups was not significantly different (by Levene's Test).

Pre-processing (cell extraction). Time series data sets were *x*-*y* motion corrected with ImageJ plug-in Stack Reg using rigid body transformations. Cell extraction was then performed sequentially, by first computing cell segments automatically followed by manual quality control for missed cells, non-cells, or conjoined cells. For initial automatic extraction, we used a metric based on image threshold intensity, variance and skewness. Images with high contrast-to-noise ratio, wherein clear thresholds in maximum intensity separated cells and background, were fully segmented with the former. In the remainder of cases, cells were distinguished from background based on standard deviation across time (high for active cells), or skewness (asymmetry) in intensity across time⁵³. This resulted in a general mathematical criterion to define cell-masks at each voxel location (*i,j,k*):

$$M(i,j,k) = \alpha_F I(F_{\max}(i,j,k) > F_c) + \beta_F I(\sigma_F(i,j,k) > \sigma_c) + \gamma_F I(s_F(i,j,k) > s_c)$$

where *I* is the indicator function (=1 if the condition is satisfied); $\sigma_F(i,j,k)$ is the standard deviation of intensity over time defined as

$$\sigma_F^2(i,j,k) = E[(F(i,j,k,t) - \bar{F})^2]$$

and skewness is defined as

$$s_F(i,j,k) = E\left[\left(\frac{F(i,j,k,t) - \bar{F}}{\sigma_F(i,j,k)}\right)^3\right]$$

E is the expectation operator; F_c , σ_c and s_c represent cut-offs for image intensity, standard deviation and skewness respectively. Coefficients α_F , β_F and γ_F are chosen on an image-specific basis; if thresholding is sufficient β_F and γ_F are chosen to be zero, otherwise coefficients are iterated to obtain a cell mask containing the largest population of active cells (evaluated by inspection).

Automatic cell extraction was then followed by manual cell-by-cell curation to identify cells that were not extracted using the automated algorithm. This occurs when cell boundaries may not be captured due to non-translational motion artefact in the original imaging, and/or lack of clear cut-offs F_c , σ_c and s_c differentiating cell and background. For these cases, cell detection is performed with a manual editing step involving comparison of the automated cell-mask to the raw image data, and by using a Gaussian filter was applied on the edited image to smooth edges, and edge-detection⁵⁴ was used to define cell boundaries. The interior of the resulting cells were filled, and the final cell masks were eroded to minimize contamination from neuropil signal. Each cell was labelled with a unique cell identifier for the next stage; custom-written MATLAB scripts were used for all steps, and are available on request.

Processing. Calculation of $\Delta F/F$. For each cell identified in step 1, the intensity value *F* was obtained by averaging over all pixels inside the ROI to compute a space-averaged value \bar{F} for each frame (corresponding to a single time point). These are used to define $\Delta F/F$ in each cell as

$$\frac{\Delta F}{F} = \frac{\bar{F} - \bar{F}_{\text{baseline}}}{\bar{F}_{\text{baseline}}}$$

where $\bar{F}_{\text{baseline}}$ is the baseline fluorescence, calculated as the mean of the fluorescence values for a given cell, continuously acquired over a 20 s moving time window to account for slow time-scale changes in fluorescence. Given the sparse firing of neurons in our data set, the mean served as an accurate estimate of baseline activity (fluorescence). Furthermore, the main results of the study were not influenced by using the median or 8th percentile as the baseline (and correlations were independent of baseline definition).

Statistical analysis of neuronal responses. We used an approach similar to that outlined previously³⁴ to identify significant transients in each neuron, as well as to estimate and remove effects that may be related to motion artefacts. Briefly, to estimate the occurrence rate of potential motion-related fluorescence changes in the signal, all negative deflections in the $\Delta F/F$ trace were assumed to be due to motion. Because motion-related fluorescence changes should be equally likely to generate positive- or negative-going changes, positive and negative deflections in the $\Delta F/F$ curve that are attributable to motion should occur at the same frequency and can be subtracted out of the signal by using the rate of occurrence of the negative-going transients as an estimate of the rate of motion-related positive-going transients.

To determine statistically significant transients, we first calculated an estimate of the noise for each cell using an iterative approach: (1) initialize a cut-off value that separates signal and noise, (2) calculate the standard deviation (σ) of all $\Delta F/F$ values that fall below the cut-off, and (3) compare 3σ to the cut-off. In this analysis, the goal is to find an estimate of standard deviation (σ) of the noise, defined for time periods that are unlikely to contain neural events (that is, using the iterative approach to estimate the σ of the noise, rather than calculate standard deviation for the entire time epoch, which would contain real events). For each iteration of the analysis, if $| \text{cut-off} - 3\sigma | < \text{tolerance}$, the program terminates (where tolerance = 0.02). If $\text{cut-off} > 3\sigma$, the program increases the cut-off by 10% and goes back to step 1. If $\text{cut-off} < 3\sigma$, it reduces the cut-off by 10% and goes back to step 1. This approach helped ensure that neuronal activity-generated events in $\Delta F/F$ are not included in the estimation of noise and avoided the need for manually selecting epoch intervals on a cell-by-cell basis that did not contain an event in order to estimate noise.

Subsequently, we analysed positive- and negative-going transients to further determine the false positive rate. Transient onsets are defined as the times when the $\Delta F/F$ exceeds 2σ and offset is defined as the time at when a given transient falls below 0.5σ . A histogram of the number of transients that exist for each σ threshold value (that is, $>2\sigma$, $>3\sigma$, $>4\sigma$), for various durations, is extracted, where negative-going transients are to the left of the ordinate and plotted in red (Extended Data Fig. 4c–f). The ratio of the number of negative to positive going transients is calculated for different transient durations across three amplitude levels (2σ , 3σ , 4σ), and serves as our estimate of false positive rate. Following from the reasoning described earlier, this ratio will be 50% when the motion-based noise significantly exceeds the signal. We plot the false positive ratio for the different scenarios described earlier, and choose the amplitude (in σ) and duration cut off (Extended Data Fig. 4c–f) needed to reduce the false positive rate to below 5%. As mentioned previously³, it is important to note that this estimate of noise represents an upper bound, and could be influenced by other sources of noise apart from motion (that is, photon shot noise).

Calculation of correlation coefficients between neuron pairs. The Pearson correlation coefficient was calculated between each pair of cells, c_a and c_b , as

$$\rho_{c_a, c_b} = \frac{E((c_a - \bar{c}_a)(c_b - \bar{c}_b))}{\sigma_{c_a} \sigma_{c_b}}$$

This metric measures linear dependence between signals in the two cells, and is invariant with respect to scaling or amplitude translation of the cell signals. We define a matrix of correlation coefficients of size $N_{\text{cells}} \times N_{\text{cells}}$ wherein each entry corresponds to correlation between the cells identified by the corresponding row and column. To avoid accumulation in correlated signal due to slow drifts (for example, the long decay curve of GCaMP6m), we set all $\Delta F/F$ values lying outside the window of a significant transient (as defined earlier) to 0.

Post-processing. Histogram of cell activity correlations. The property of high correlation (HC) was tested for in each neuron by finding the number of correlated neurons with which the Pearson's correlation coefficient was above 0.3 (a Pearson correlation cut-off of 0.3 was used as a conservative estimate of connectivity since previous studies using *in vivo* two-photon calcium imaging followed by paired whole-cell recordings reported a greater than 50% chance of connectivity when correlations of Ca^{2+} signals exceeded 0.3 *in vivo*)^{55,56}. Histograms were obtained by binning this number across neurons in steps of 5 and calculating the number of neurons that fell into each bin, with the resulting histogram representing the degree distribution of all neurons in the network.

HC neurons were defined as those neurons that had more correlated partners than that of the average neuron in the same volume by >1 standard deviation. **Optimally separating hyperplane.** To identify network population activity measures that best distinguished fear and neutral contexts, we used a space of graph theoretic parameters (described later), which together can be used to define an optimally separating hyperplane between the two contexts. Mathematically, this is posed as a constrained optimization problem, with the objective function seeking to maximize the sum of distances of the hyperplane to the nearest data points in each context, and the constraint being that the hyperplane separates the two contexts. This constrained optimization problem was solved using Lagrange multipliers.

Synchrony and quantification of lead-lag. To analyse the spontaneous activity of the entire network, we computed the onset and duration of each activity transient (where event onsets and offsets are calculated as described earlier) for each neuron, and then combined transients from all cells into raster plots and collapsed these raster plots into activity histograms, which indicated the percentage of active cells as a function of time.

To identify epochs of synchronous activity that included more active cells than would be expected by chance at each frame, we used interval reshuffling (randomly reordering of intervals between events for each cell), performed 1,000 times for each mouse in each context, such that a surrogate histogram was constructed for each reshuffling. The threshold percentage of active neurons corresponding to a significance level of $P < 0.05$ (appearing only in 5% of histograms) was taken to be the per cent of coactive cells required in a single frame to be considered a synchronous event, and this threshold ranged between 2.5% and 5% active neurons per frame across all mice and fields of view. At least three consecutive frames with activity above the significance threshold were required to be considered a synchronous event, and all subsequent contiguous frames above this threshold were grouped together into the same synchronous event. To plot the cumulative distribution function of event onsets for HC and non-HC neurons during synchronous events, all synchronous events across all mice were identified, and the onset times of HC versus non-HC neurons were binned per frame and plotted cumulatively as a function of the percentage of time elapsed during the synchrony window.

To quantify whether the activity of HC neurons was leading or lagging their correlated pairs, the event onset of the HC neurons (defined as the first instance when the signal exceeded 3σ for time consecutive frames) was first fixed at $t = 0$. The event onsets of all correlated pairs were then binned into 0.167 s time windows immediately preceding or succeeding the onset of the hub neuron at $t = 0$.

PCA. PCA was used to describe and visualize population activity of all neurons over time in each context. This was done by transforming the $\frac{\Delta F}{F}$ of each cell (typically ~ 500 cells per mouse per context), over all time points in a given context (typically 1,800 frames) to a different coordinate system characterized by linearly independent eigenvectors, where each eigenvector represents a weighted combination of the different cells. Eigenvalues were sorted in decreasing order to reveal the most energetic (contributory) eigenvectors as well as the magnitude of their overall contribution. PCA was performed using eigenvalue decomposition of the correlation matrix. The corresponding eigenvalues and eigenvectors were calculated using custom MATLAB scripts.

Estimation of graph-theoretic parameters. An undirected graph is defined based on the cell correlations in the population. An edge, E , is defined between neurons if they are correlated beyond the threshold described earlier. The undirected neuronal graph $G(V, E)$ is defined using all the cells, which are denoted by V (vertices), and E (edges). Mean and maximum cell correlations are calculated using aggregate average and the maxima over all of the measured correlations. We also fit an exponential distribution between n_{corr} (the number of correlations) and n_{freq} (the degree distribution described earlier) to quantify how closely the graph mimics small world networks, which are characterized by a power law degree distribution

$$n_{\text{freq}} = a(n_{\text{corr}})^{-b}$$

for which the power law parameters, a and b , are calculated by transforming the above equation into a logarithmic scale and performing a minimum least-squares fit.

A neighbourhood is defined for each cell as a sphere of radius 30 μm . The clustering coefficient for a vertex is defined as the ratio of number of edges within its neighbourhood to the maximum number of connections possible. If there are k nodes in the neighbourhood, $k(k-1)/2$ is the maximum number of possible connections⁹. The clustering coefficient of the entire network is defined as the mean clustering coefficient across all vertices. The mean path length is defined as the average path between any two randomly selected vertices of the graph. The

mean path length (mpl) is calculated by first constructing an adjacency matrix, which is an $n_{\text{cell}} \times n_{\text{cell}}$ matrix, and all correlated vertex pairs are given a value of one in the corresponding row and column, and zero otherwise. The minimum path from i to j can be recursively calculated using

$$\text{mpl}_{i,j} = \min(\text{mpl}_{i,k} + \text{mpl}_{k,j})$$

Small-world networks are characterized by high clustering coefficient and low mean path length, quantified using the ratio of clustering coefficient to mean path length, where each term is normalized to a purely random graph with the same number of vertices. Betweenness centrality is a measure of the centrality of nodes in the network, and indicates how central a node is to communication between all pairs of node. Betweenness centrality is computed by calculating all possible paths between two nodes and calculating the number of those that pass through a given node. Strength of a graph quantifies how strongly different subcomponents of a graph are connected and is a measure of resistance of the graph to attack on its edges. Let $P = (V_1, V_2 \dots V_n)$ denote all possible partitions of the graph G into a mutually exclusive set of vertices $V_1, V_2 \dots V_n$, such that the union of all the vertices is V . Let E_r denote the number of edges that needs to be removed from G to create the partition P . Then the strength is defined as $s = \min \frac{E_r}{n-1}$, where the minima are calculated over all possible partitions P . In other words, the strength quantifies how to remove minimal edges to create maximal separation among vertices of the graph. The strength is calculated using MATLAB code based on algorithms described previously^{57,58}.

Fast non-negative deconvolution algorithm implementation. Deconvolution algorithms enable the estimation of spike rate trains from fluorescence data. Here, we use deconvolution to estimate activity-event onset, not to detect single spikes, since GCaMP6m is assumed to neither have the linear response kinetics nor the sensitivity needed to detect single spikes from bursting neurons in the hippocampus. We used this analysis to help confirm our main results regarding synchronous events and timing of highly correlated neurons, since these analyses offer an alternative method to identify event onsets, while helping to remove noise (for example, long Ca^{2+} signal decays) from the analyses.

Many deconvolution algorithms exist. Early methods to deconvolve fluorescence data used either thresholding to infer event onset⁵⁹ or optimizations to match a chosen spike profile⁶⁰. More robust algorithms such as the Wiener linear filter are promising⁶¹ but with practical value diminished since negative-going spikes are allowed. In 2010, Vogelstein and colleagues provided a fast non-negative deconvolution method that is, in addition to imposing a non-negative constraint on the spike trains, scalable on a large population of neurons³². Since our imaging involves hundreds of neurons over multiple contexts and days, we use the algorithm from Vogelstein *et al.* to deconvolve fluorescence signals.

Three classes of parameters were optimized in this algorithm to fit data: (1) GCaMP-related parameters, namely sensitivity of fluorescence to elevations in intracellular Ca^{2+} concentration (α) and baseline concentration (β); (2) acquisition parameters, namely the size of the time bin (δ) and the noise (σ) in the $\Delta F/F$ signals; and (3) system (hippocampus/CA3)-related parameters, namely expected spike rate per second (φ) and the time constant (τ), or the length it takes for Ca^{2+} concentrations to decay. For the GCaMP-related parameters, β is set to the baseline of the $\Delta F/F$ traces as described earlier, and α is set to 1 as a default value (since varying α broadly around this value did not affect the deconvolution results). δ was set to 1/3 s because image acquisition was at least 3 Hz per optical slice, and σ was estimated to be 0.16 as explained earlier. The main challenge resides in choosing parameters for φ and τ since (1) the expected spike rate (close to 0.1 Hz on average, but >10 Hz when bursting) is bimodal and insufficiently captured by the Poisson distribution of spikes as assumed by this model, and (2) the time constant expected for Ca^{2+} signals in hippocampus is not fully understood. Therefore, we optimized these two parameters by iterating over multiple combinations of time constants and expected spike rates to yield spike events consistent with good fits to our data (Extended Data Fig. 8). The final parameters chosen were: $\alpha = 1$; $\beta = \text{baseline}$; $\delta = 0.33$ s; $\sigma = 0.16$; $\varphi = 5$ Hz; $\tau = 2$ s. These values were not exactly the same as, but were comparable to, values reported by others in cortical regions^{49,55,62}. Importantly, varying φ and τ within a fairly broad range ($\varphi \sim 5\text{--}10$ and $\tau \sim 0.67\text{--}2$) did not significantly alter the main conclusions of the subsequent analyses. The $\Delta F/F$ signals for all the mice, contexts and days were deconvolved. Correlation coefficients were calculated on the deconvolved signals, and metrics that rely on accurate estimate of event onsets were recomputed, such as synchrony, lead-lag, and identification of HC neurons. The only difference from the methods described earlier was that there were no additional noise filters since the noise is filtered in the process of finding the optimal spike rate (here, event rate), and the onset time was characterized by the first instance that the signal became non-zero. Further analysis of the various specific deconvolution parameters would be of interest but would probably require combined

in vivo imaging and single-cell patching experiments, beyond the scope of the current study, and unlikely to significantly affect the specific analyses applied here given the robustness of results to broad ranges of parameters. Furthermore, we performed the analyses described earlier only to help ensure robustness in results obtained from using the raw $\Delta F/F$ for measurements relying on precise timing (correlations, leading versus lagging, and synchrony).

Virtual reality behavioural analysis. Lick rates and movements on the ball were captured in XML log files storing timestamps of behavioural data. These were then parsed with custom Python scripts and imported into MATLAB for synchronizing with microscope imaging frames with kHz precision, and for subsequent analysis. To quantify differences in licking between fear and neutral contexts during retrieval, the number of licks per second (each lick causing a beam-break resulting in TTL pulse output of at least 1V), was integrated over the first 2 min in the context. Total licking amounts were normalized to the highest lick rate, observed from any mouse in any context, and presented as a fraction of this value for each mouse and each context. Lick suppression data are presented as mean values across all mice in each experimental group; significance values of differences between contexts were evaluated by Student's *t*-test. Lick rates during optogenetic stimulation experiments were scored by quantification during the 15 s of light delivery, which was then normalized to the corresponding value from the 15 s just before light delivery. Significant differences in licking for fear versus neutral context, and for neutral/stimulated versus neutral context alone, were evaluated using Student's *t*-test. Lick rates and velocity on ball during synchronous population activity events were calculated by comparing the amount of licking and distance travelled in the 5 s window beginning at the start of a synchronous event, and then normalizing to the amount of licking and distance travelled in the 5 s window before synchronous event. Similar quantitative results were observed with this time window set to 1–10 s after synchrony compared with before, with no significant difference in lick rate and velocity during versus before synchrony.

Simultaneous 1P *in vivo* stimulation and 2P *in vivo* imaging. Simultaneous 1-photon (1P) stimulation (594 nm) and 2-photon (2P) imaging (920 nm) was performed by injecting the new red-shifted opsin with improved trafficking and kinetics (bReaChES) via AAV8 in cingulate and GCAMP6m via AAVdj in CA3, and positioning a cranial window above CA2/CA3 for optical access. The 2P imaging and full-field optogenetic stimulation setup is shown in Fig. 4b. Briefly, a resonant galvanometer 2P microscope using an NIR pulsed laser set to 920 nm is combined with simultaneous, full field stimulation using a 594 nm continuous wave laser that is coupled into the system with an optical fibre, lenses and dichroic beam splitters. A 2P compatible NIR reflecting dichroic designed with an additional 594 nm band-pass filter was used for 1P yellow light stimulation during 2P imaging. GCaMP6m signals (green channel) and stimulation artefact (red channel—used to precisely blank stimulation time points) are recorded using standard 2P resonant scanning imaging. 1P stimulation artefacts were removed offline from the 2P images. Stimulation parameters: 591 nm light, 20 Hz, 15 ms pulses, 15 s, 8–10 mW mm⁻² laser power at sample after the objective. In total, 4 mice (separate cohort from those used in the imaging-only experiments) were used for the combined stimulation and imaging experiments. The same cells and the same FOV are captured for before-training stimulation trials as well as after-training stimulation trials (conducted 5–7 days later). For a neuron to be considered responsive to (recruited by) the stimulus, at least one significant transient as defined earlier was required to occur during the stimulation window. For latency measurements provided in Fig. 4, event onsets were defined as the first time frame at which the response surpassed three standard deviations above noise, and increased for at least two consecutive frames; if occurring within the first frame, then only neurons with responses increasing from the previous frame are considered, to exclude responses decaying into the stimulation window. Responding neurons were assigned to latency bins of 333 ms.

DSI electrophysiology. DSI is dependent on the increase of postsynaptic intracellular Ca^{2+} to suppress GABA release from presynaptic inhibitory neurons expressing cannabinoid receptors⁶³. We performed patch-clamp recordings from CA3 neurons expressing GCaMP6m and examined spontaneous inhibitory postsynaptic currents (sIPSCs) before and following a depolarizing pulse to induce Ca^{2+} influx. Electrophysiological recordings were performed 4–6 weeks post-injection of AAVdj-CaMKIIα::GCaMP6m into CA3 (in 4–5-week-old mice). Coronal slices (300 μm) from injected mice were prepared after intracardial perfusion with ice-cold, sucrose-containing artificial cerebrospinal fluid solution (ACSF; in mM): 85 NaCl, 75 sucrose, 2.5 KCl, 25 glucose, 1.25 NaH_2PO_4 , 4 MgCl_2 , 0.5 CaCl_2 and 24 NaHCO_3 . Slices recovered for 1 h at 32–34 °C, and then were transferred to an oxygenated recording ACSF solution (in mM): 123 NaCl, 3 KCl, 26 NaHCO_3 , 2 CaCl_2 , 1 MgCl_2 , 1.25 NaH_2PO_4 and 11 glucose, at room temperature. Excitatory synaptic transmission blockers (D-2-amino-5-phosphonovaleric acid (APV; 25 μM) and 2,3-dihydroxy-6-nitro-7-sulfamoyl-benzo[f]-quinoxaline-2,3-dione (NBQX; 10 μM) were added to isolate GABAergic

postsynaptic currents, and 5 μM carbachol was used to enhance sIPSC frequency to facilitate detection of DSI. Recordings were performed at 32–34 °C under constant perfusion of the oxygenated recording ACSF solution. Slices were visualized with an upright microscope (BX61WI, Olympus) under infrared differential interference contrast (IR-DIC) optics, and a Spectra X Light engine (Lumencor) was used for viewing GCaMP6m expression. Recordings of CA3 neurons were made after identifying GCaMP6m expression, and functional GCaMP6m activity was verifiable (in cells without BAPTA), by observing the increase in GCaMP6m fluorescence during the depolarizing pulse used to induce DSI. The following intracellular solution was used for the patch-clamp electrodes (in mM): 40 CsCl, 90 K-Gluconate, 1.8 NaCl, 1.7 MgCl₂, 3.5 KCl, 10 HEPES, 2 MgATP, 0.4 Na₂GTP, 10 phosphocreatine (pH 7.2, 270–290 mOsm). For the BAPTA experiments, 40 mM BAPTA was added to the intracellular solution. Series resistance was monitored for stability, and recordings were discarded if the series resistance changed significantly (by >20%) or reached 20 MΩ. Resting membrane potential was taken at rest, and the reported values incorporate a liquid junction potential of +11.2 mV. Input resistance was calculated from a 100 pA pulse. MiniAnalysis (Synaptosoft) and pClamp10.3 (Molecular Devices) was used to calculate charge transfer (area under sIPSCs) and analyse data. Baseline charge transfer was measured during a 4 s pre-pulse period, DSI was examined during a 4 s period following the depolarizing pulse, and charge transfer after recovery from DSI was measured during a 4 s window. The pulse used to evoke DSI was a 500 ms step to 0 mV from holding potential of −65 mV.

bReaChES design and testing

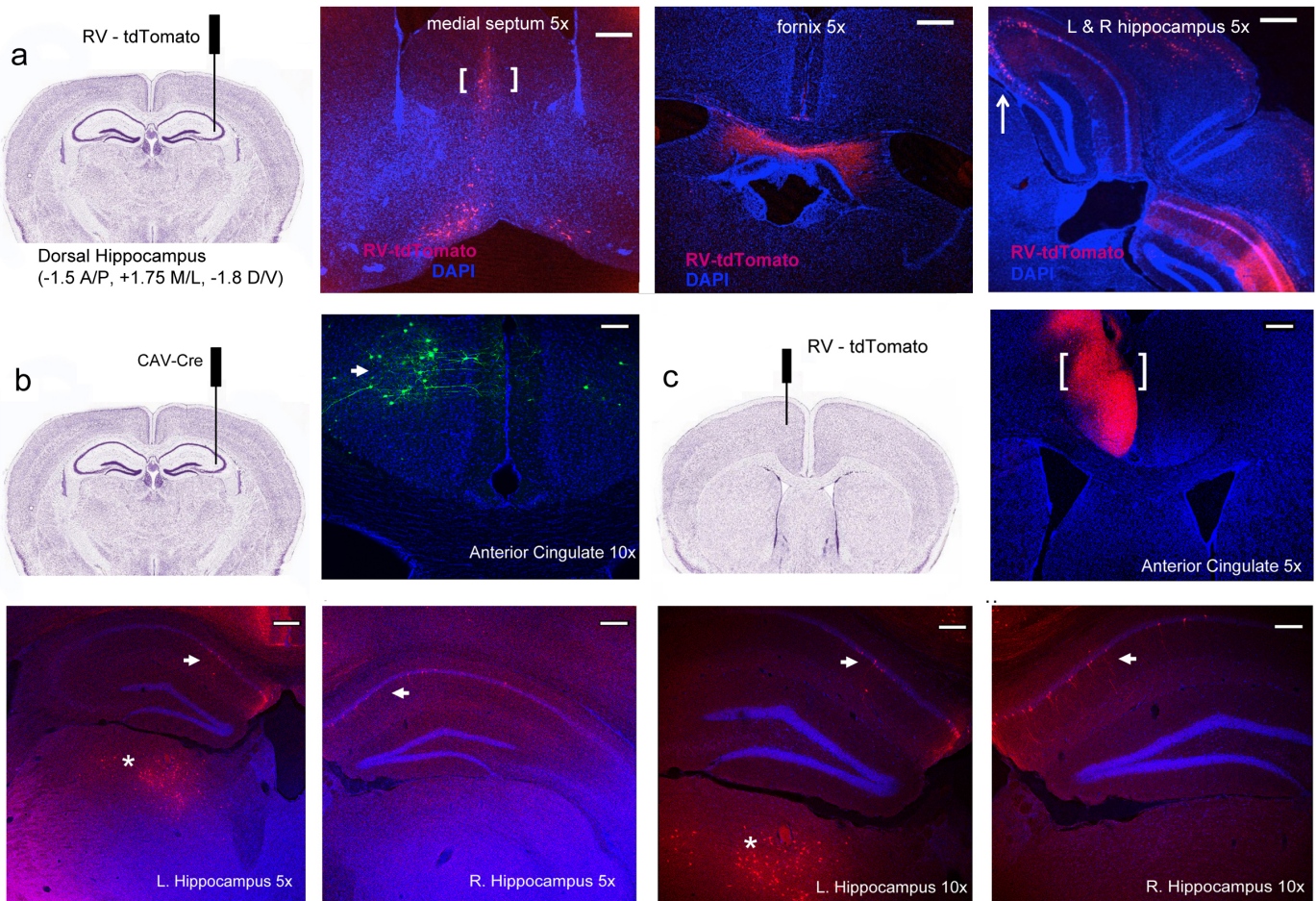
Cloning and single mutagenesis of ReaChR and bReaChES. DNA sequences of ReaChR and bReaCh were synthesized (GenScript) and cloned into AAV vectors containing the CamKIIα promoter for expression in neurons. All constructs were fused to eYFP DNA to detect protein expression in neurons by fluorescence microscopy. The Glu123Ser mutation was introduced using QuickChange Site-Directed mutagenesis kit (Agilent). Plasmid DNA was purified with QIAprep Spin Miniprep Kits (Qiagen) after transformation and amplification in *Escherichia coli*.

Electrophysiological recordings in cultured hippocampal neurons. Electrophysiological recordings in neuronal cultures were prepared as described⁶⁴. Patch pipettes (4–6 MΩ) were pulled from glass capillaries (Sutter Instruments) with a horizontal puller (P-2000, Sutter Instruments) for whole-cell recordings in voltage and current clamp. Recordings were made using a MultiClamp700B amplifier (Molecular Devices). The external recording solution contained (in mM): 127 NaCl, 10 KCl, 10 HEPES, 2 CaCl₂, 2 MgCl₂, 30 D-glucose, pH 7.3, including synaptic blockers (25 μM D-APV, 10 μM NBQX). The patch pipette solution contained (in mM): 140 K-gluconate, 10 HEPES, 10 EGTA, 2 MgCl₂, pH 7.3. All measurements were corrected for a liquid junction potential of +15 mV. Series resistance was monitored throughout recordings for stability. A Spectra X Light engine (Lumencor) was used to excite eYFP and to apply light for opsins activation. Yellow and red stimulation light was filtered by 575/25 or 632/22 band-pass filters (Chroma) and applied through a ×40 objective (Olympus) at 5 mW mm⁻² light intensity. Light power density was measured with a power meter (ThorLabs). The functionality of all constructs was determined by comparing stationary photocurrents at −80 mV to 1 s continuous light pulse. Spikes were optically evoked in current-clamp mode with light pulses (5 ms) delivered at 633 nm, 5 mW mm⁻² and 1–20 Hz. The activation spectra for C1V1, bReaCH-ES and ChR2 was measured by recording stationary photocurrent in voltage clamp mode at −80 mV and light intensities of 0.65 mW mm⁻² at each wavelength. Light was delivered through 20 nm band-pass filters (Thorlabs) at (in nm): 400, 420, 440, 460, 470, 480, 490, 500, 520, 540, 560, 570, 580, 590, 600, 620, 630, 650. Photocurrents were normalized to maximum values respectively: 480 nm for ChR2, 560 nm for C1V1 and 570 nm for bReaCH-ES. Kinetics of channel closure were determined by fitting the decay of photocurrents after light off, with mono-exponential functions. Channel kinetics were quantified by corresponding τ_{off} values respectively. pClamp10.3 (Molecular Devices) and OriginLab8 (OriginLab) software was used to record and analyse data.

Stereotactic virus injection of bReaCh-ES. The following adeno-associated viruses (AAVs) with serotype DJ were produced at the Stanford Neuroscience Gene Vector and Virus Core: AAVDJ-CaMKII::bReaCh-E162S-TS-eYFP; and AAVDJ- CaMKII::C1V1(E122T/E162T)-TS-eYFP. Four-to-six-week-old mice were injected bilaterally with 1 μl of either virus in the medial prefrontal cortex, at the following coordinates (from Bregma): A/P: +1.7 mm; M/L: +0.3 mm; D/V: −2.5 mm. Titre was matched at 1.5×10^{12} vg ml⁻¹ for both viruses.

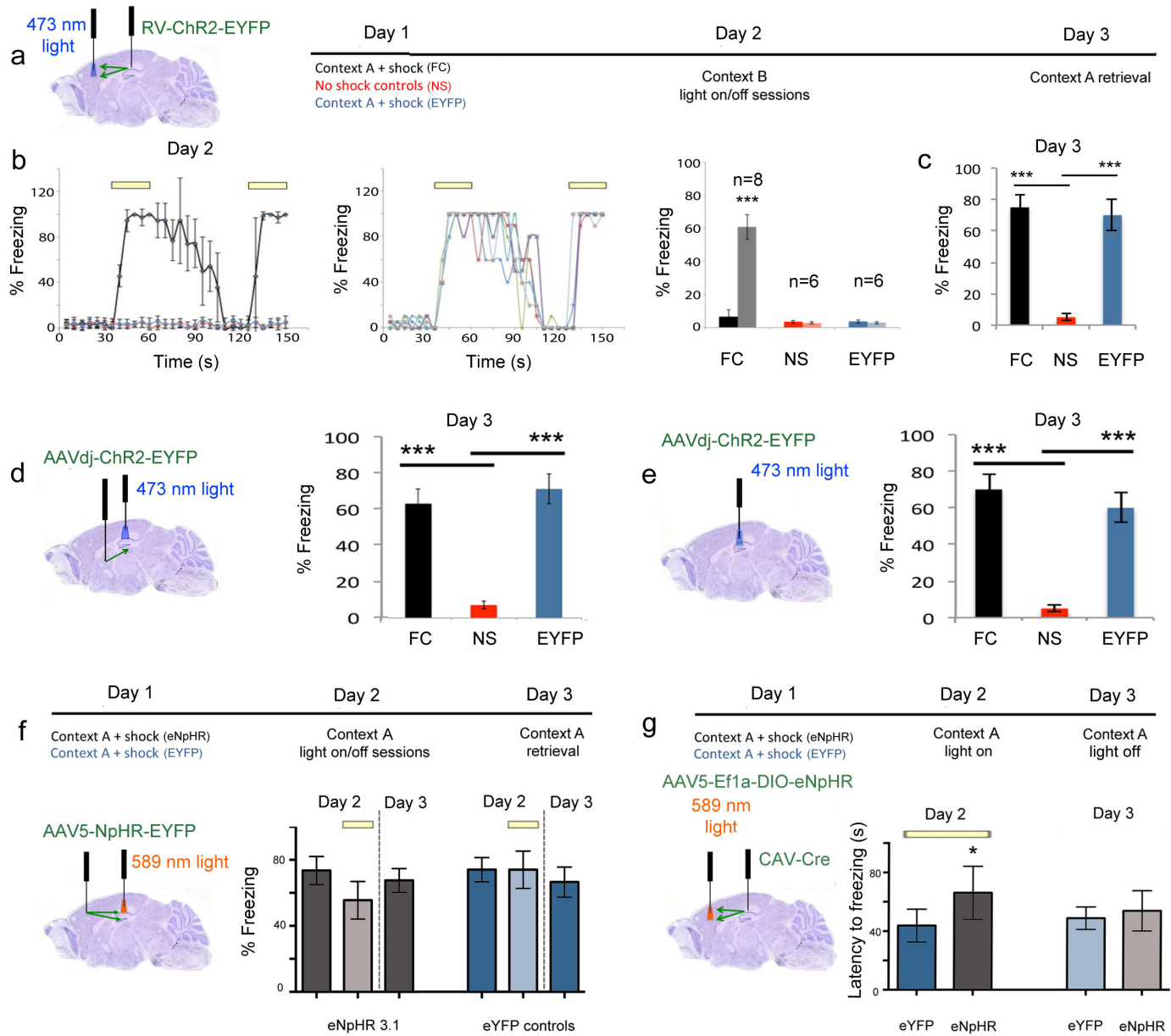
Slice electrophysiology for bReaCh-ES characterization in mPFC and BLA. Electrophysiological recordings were performed 12–14 weeks post-injection for opsins expression at the mPFC terminals. Coronal slices (300 μm) from injected mice were prepared after intracardial perfusion with ice-cold, sucrose-containing ACSF (in mM): 85 NaCl, 75 sucrose, 2.5 KCl, 25 glucose, 1.25 NaH₂PO₄, 4 MgCl₂, 0.5 CaCl₂ and 24 NaHCO₃. Slices recovered for 1 h at 32–34 °C, and then were transferred to an oxygenated recording ACSF solution (in mM): 123 NaCl, 3 KCl, 26 NaHCO₃, 2 CaCl₂, 1 MgCl₂, 1.25 NaH₂PO₄ and 11 glucose, at room temperature. Electrophysiological recordings were performed at 32–34 °C under constant perfusion of the oxygenated recording ACSF solution. For mPFC recordings, synaptic transmission blockers (APV (25 μM), NBQX (10 μM) and gabazine (10 μM)) were added to the recording ACSF solution. Slices were visualized with an upright microscope (BX61WI, Olympus) under IR-DIC optics. A Spectra X Light engine (Lumencor) was used both for viewing fluorescent protein expression and delivering light pulses for opsins activation. Light power density was obtained with a power meter (Thorlabs). Recordings of mPFC neurons were made after first identifying regions of eYFP⁺ expression, and recordings of postsynaptic basolateral amygdala (BLA) neurons were obtained after confirming eYFP⁺ expression in both mPFC and the mPFC axonal fibres at the BLA. Whole-cell voltage-clamp recordings were performed at −65 mV, and current-clamp recordings were performed at rest. Patch-clamp pipettes contained the following internal solution (in mM): 125 K-gluconate, 10 KCl, 10 HEPES, 4 Mg₃-ATP, 0.3 Na-GTP, 10 phosphocreatine, 1 EGTA. Recordings were conducted using MultiClamp700B amplifier and pClamp10.3 software (Molecular Devices). pClamp10.3, OriginLab8 (OriginLab), and SigmaPlot (SPSS) were used to analyse data. Stationary photocurrent of the opsins was measured at the end of a 1 s light pulse in voltage-clamp mode. Light-evoked spike probability in the mPFC neurons and in the postsynaptic BLA neurons was calculated as the fraction of successful action potentials evoked in the recorded neuron upon various light stimulation frequencies. Light-evoked EPSC amplitude in the postsynaptic BLA neurons was measured at the peak of the evoked response to light stimulation of the opsin-expressing mPFC fibres. Series resistance was monitored for stability, and recordings were discarded if series resistance changed significantly (by >20%) or reached 20 MΩ. Statistical analysis was performed with two-tailed t-test, with significance set at $P < 0.05$.

51. Harvey, C. D., Coen, P. & Tank, D. W. Choice-specific sequences in parietal cortex during a virtual-navigation decision task. *Nature* **484**, 62–68 (2012).
52. Niell, C. M. & Stryker, M. P. Modulation of visual responses by behavioral state in mouse visual cortex. *Neuron* **65**, 472–479 (2010).
53. Mukamel, E. A., Nimmerjahn, A. & Schnitzer, M. J. Automated analysis of cellular signals from large-scale calcium imaging data. *Neuron* **63**, 747–760 (2009).
54. Cann, J. A computational approach to edge detection. *IEEE Trans. Pattern Anal. Mach. Intell.* **8**, 679–698 (1986).
55. Ko, H. et al. Functional specificity of local synaptic connections in neocortical networks. *Nature* **473**, 87–91 (2011).
56. Cossel, L. et al. Functional organization of excitatory synaptic strength in primary visual cortex. *Nature* **518**, 399–403 (2015).
57. Tarjan, R. E. Depth first search and linear graph algorithms. *SIAM J. Comput.* **1**, 146–160 (1972).
58. Sedgewick, R. *Algorithms in C++, Part 5 Graph Algorithms* (Addison-Wesley, 2002).
59. Schwartz, T. H. et al. Networks of coactive neurons in developing layer 1. *Neuron* **20**, 541–552 (1998).
60. Greenberg, D. S., Houweling, A. R. & Kerr, J. N. Population imaging of ongoing neuronal activity in the visual cortex of awake rats. *Nature Neurosci.* **11**, 749–751 (2008).
61. Holekamp, T. F., Turaga, D. & Holy, T. E. Fast three-dimensional fluorescence imaging of activity in neural populations by objective-coupled planar illumination microscopy. *Neuron* **57**, 661–672 (2008).
62. Smith, S. L. & Häusser, M. Parallel processing of visual space by neighboring neurons in mouse visual cortex. *Nature Neurosci.* **13**, 1144–1149 (2010).
63. Castillo, P. E., Younts, T. J., Chávez, A. E. & Hashimoto, Y. Endocannabinoid signaling and synaptic function. *Neuron* **76**, 70–81 (2012).
64. Berndt, A., Lee, S. Y., Ramakrishnan, C. & Deisseroth, K. Structure-guided transformation of channelrhodopsin into a light-activated chloride channel. *Science* **344**, 420–424 (2014).
65. Lee, S. Y., Földy, C., Szabadics, J. & Soltesz, I. Cell-type-specific CCK2 receptor signaling underlies the cholecystokinin-mediated selective excitation of hippocampal parvalbumin-positive fast-spiking basket cells. *J. Neurosci.* **31**, 10993–11002 (2011).
66. Kohara, K. et al. Cell type-specific genetic and optogenetic tools reveal hippocampal CA2 circuits. *Nature Neurosci.* **17**, 269–279 (2014).
67. Varga, C., Lee, S. Y. & Soltesz, I. Target-selective GABAergic control of entorhinal cortex output. *Nature Neurosci.* **13**, 822–824 (2010).



Extended Data Figure 1 | Anatomical characterization of the AC-CA projection. **a**, Five days after RV-tdT injection into the hippocampus (coordinates specified), retrogradely labelled neurons were detected in the contralateral hippocampus (arrow), medial septum (bracket), and AC (Fig. 1a). Scale bars: $\times 5$: 300 μm ; $\times 10$: 100 μm (confocal). **b**, Eight weeks after injection of CAV-Cre into the hippocampus and DIO-eYFP in the AC (coordinates specified), afferent cell bodies were detected in the AC (arrow). Confocal image;

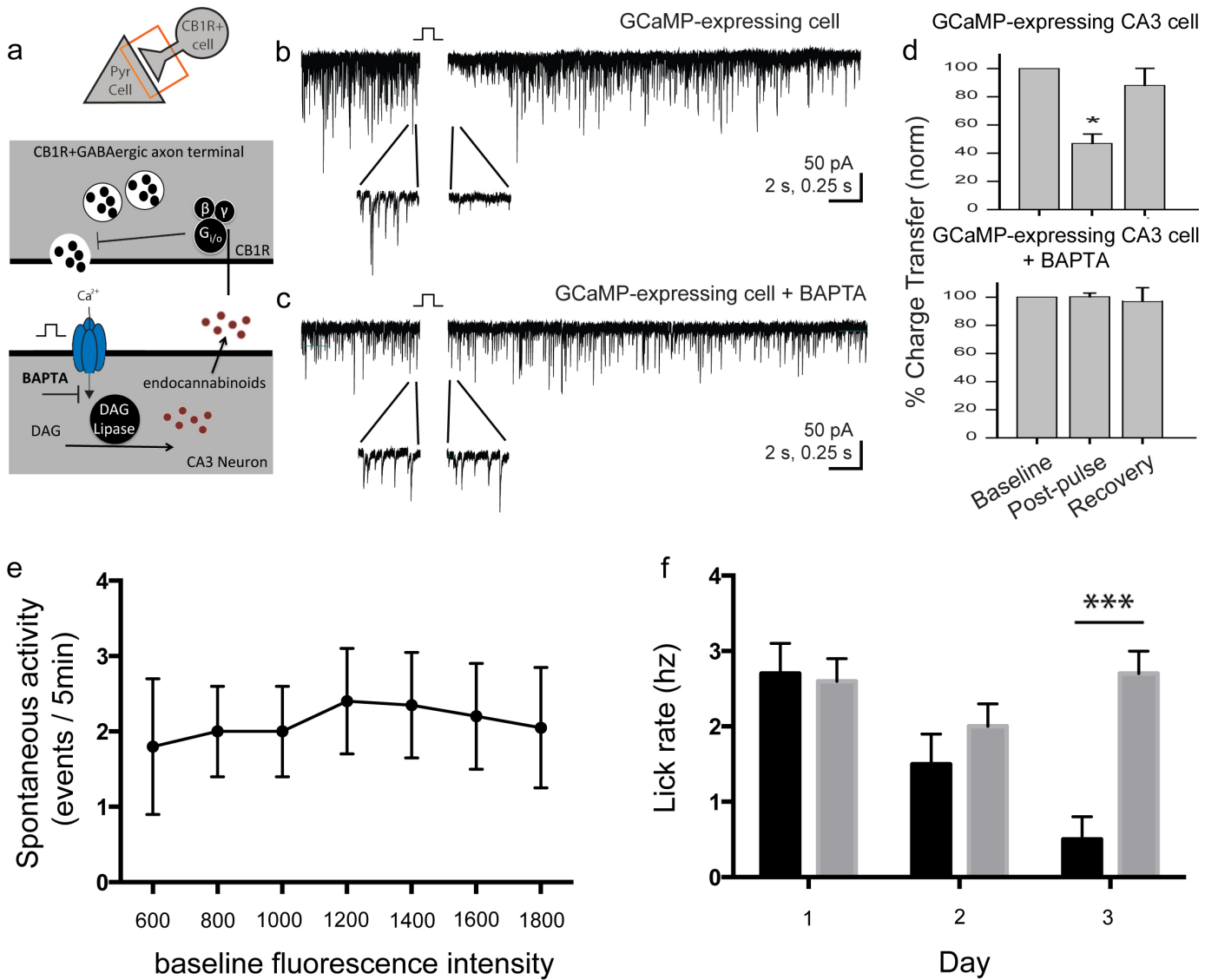
$\times 10$ magnification; scale bar: 100 μm . **c**, Retrograde tracing with RV-tdT from the AC to map reciprocal connections from the hippocampus. The injection site is indicated in brackets, sparse labelling of afferent cell bodies in left and right hippocampus, primarily in the subiculum (arrows), and also in the medial dorsal thalamic nucleus as expected (asterisk). Confocal $\times 5$, scale bar, 200 μm ; $\times 10$ images, scale bar 100 μm .



Extended Data Figure 2 | Optogenetic manipulation of the AC–CA projection.

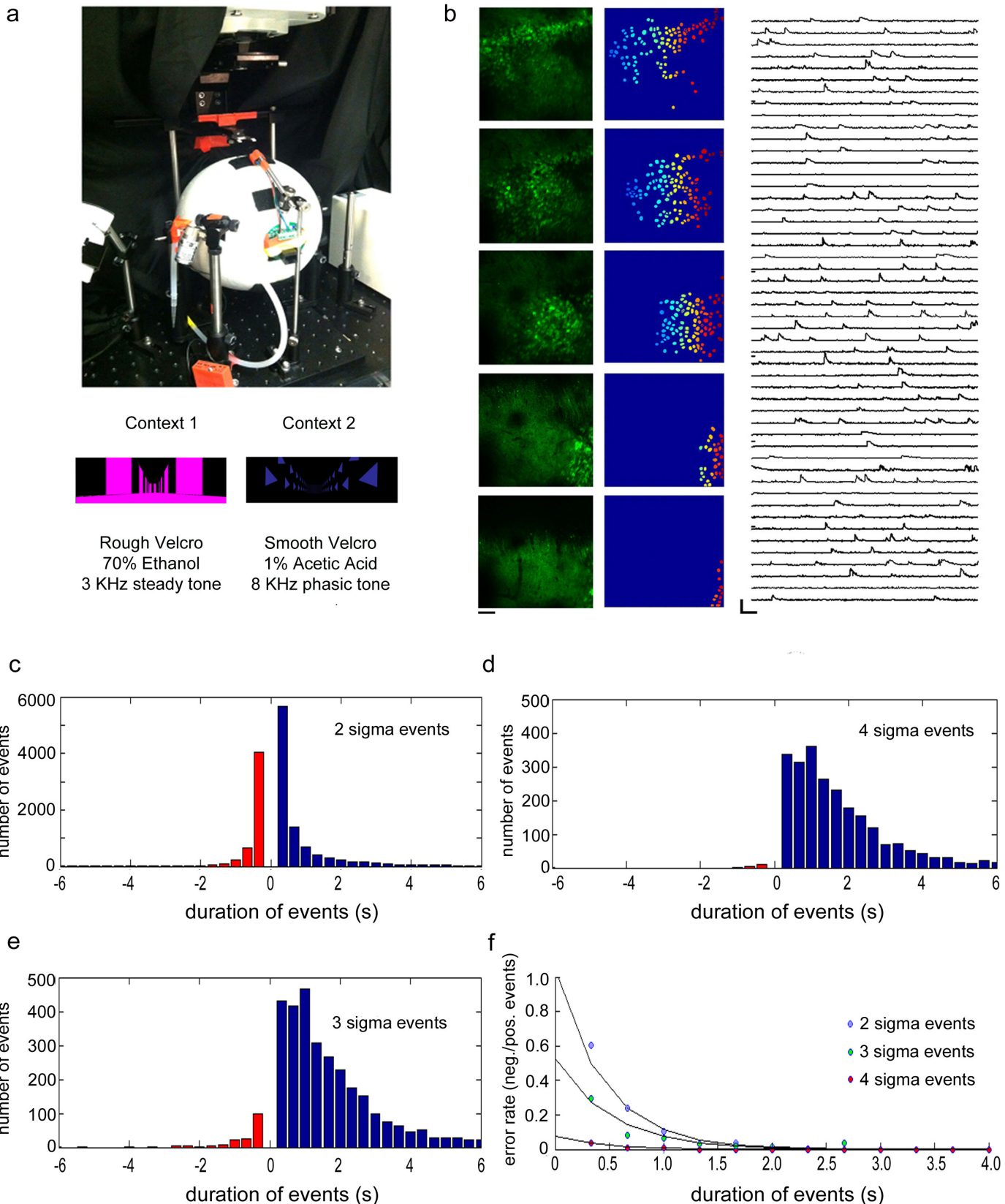
a, Experimental design: RV-ChR2-eYFP (or eYFP alone) was injected into the dorsal hippocampus and light was delivered above the cell bodies in the AC. Five days after injection, ChR2 and eYFP mice were fear conditioned in context A while no-shock controls were only exposed to context A (day 1). All mice were tested with light on and off sessions in context B (day 2), and then tested for contextual memory retrieval in context A (day 3). Optogenetic stimulation was with 473 nm light in a train of 20 Hz, 15 ms pulses, 30 s duration, with 8–10 mW laser power at fibre tip. **b**, Freezing (no head motion observed) during day 2 is plotted in 5 s time bins over 150 s in context B (left). ChR2/shock (FC): black; ChR2/no shock (NS): red; eYFP/shock (eYFP): blue. Individuals in the FC group (each animal a different colour) are shown (middle). Summary (right): percentage time freezing (mean \pm s.d.) 20 s before light on (darker shade) versus 20 s after light on (lighter shade); FC: $60.9 \pm 7.4\%$ light on versus $6.5 \pm 4.4\%$ light off, $n = 8$; NS: $2.7 \pm 0.65\%$ light on versus $3.4 \pm 0.95\%$ light off, $n = 6$; eYFP: $2.9 \pm 0.75\%$ light on versus $3.6 \pm 1\%$ light off, $n = 6$; $P < 0.001$, two-way ANOVA with repeated measures. **c**, Preservation of contextual fear memory (percentage time freezing) on day 3 in the original context (mean \pm s.d., $P < 0.001$, unpaired *t*-test). **d**, Preservation of contextual memory in medial septum injected mice (Fig. 1f); percentage time freezing on day 3 in the original context (mean \pm s.d., $P < 0.001$, comparisons shown, unpaired *t*-test). **e**, Preservation of contextual memory in hippocampus injected mice (Fig. 1h); percentage time freezing on day 3 in the original context (mean \pm s.d., $n = 8$ mice, $P < 0.001$, paired *t*-test). **f**, The successful loss-of-function experiments targeting hippocampus-dependent memory formation mediated by cells giving rise to the AC–CA projection (reported in Fig. 2) were designed to allow the most robust inhibition of this circuit element. An alternative design (attempting to target the projection field despite the broad and long septotemporal extent of the hippocampal

formation) was also explored as shown here but was not effective, as expected; we injected AAV5-eNpHR3.0-eYFP (or AAV5-eYFP in a parallel cohort) bilaterally into the AC, and targeted light stimulation bilaterally to axon terminals in the hippocampus. Eight weeks after injection, all mice were fear conditioned to context (day 1), and tested for context retrieval during light on/off sessions (day 2), and again for context retrieval in light-off only (day 3). Optogenetic inhibition was with constant illumination of 589 nm light, 30 s duration, with 8–10 mW laser power at fibre tip. **g**, We observed a trend towards reduction in freezing due to optical inhibition of the AC–CA projection during memory retrieval. Percentage time freezing in context A during day 2 before light (darker bar on left) versus after light (lighter bar at right). eNpHR3.0: $73.5 \pm 8.5\%$ light off versus $55.5 \pm 11.4\%$ light on, $n = 10$; eYFP: $74 \pm 7.4\%$ light off versus $74 \pm 11.3\%$ light on, $n = 10$; percentage time freezing in context A with light off (dark bars) during day 3 is shown after dotted line. eNpHR3.0: $67.5 \pm 7.2\%$, $n = 10$; eYFP: $66.5 \pm 9.1\%$, $n = 10$ ($P = 0.067$, two-way ANOVA). As expected, point illumination may be less effective for inhibiting broad axon terminal field volumes. **h**, Extension of findings from effective loss-of-function experiments (Fig. 2) targeting hippocampus-dependent memory formation mediated by cells giving rise to the AC–CA projection: significant effect on speed of onset of memory expression. Experimental design: CAV-Cre was injected into the dorsal hippocampus, DIO-eNpHR3.0 (or DIO-eYFP) was injected into the AC, and light was delivered above cell bodies in the AC. All mice were fear conditioned in context A (day 1), tested for latency to contextual retrieval with light-on only (day 2), and then for latency to context retrieval in light-off only (day 3). **i**, Day 2: 66.1 ± 18.1 s for eNpHR3.0 ($n = 12$) versus 43.8 ± 11.1 s for eYFP ($n = 8$) during light on; day 3: 53.8 ± 13.7 s for eNpHR3.0 versus 48.8 ± 7.7 s for eYFP during light off; $P < 0.05$ two-way ANOVA with repeated measures. * $P < 0.05$, ** $P < 0.01$, *** $P < 0.001$.



Extended Data Figure 3 | Physiological properties of GCaMP6m-expressing CA3 neurons. **a**, To ensure that expression of GCaMP6m did not alter Ca²⁺-related physiological processes, we tracked a form of endocannabinoid-mediated short-term plasticity known as depolarization-induced suppression of inhibition (DSI). Schematic diagram of DSI is shown; DSI is dependent on the increase of postsynaptic intracellular Ca²⁺ to trigger the synthesis and release of endocannabinoids, which then signal in a retrograde fashion to suppress GABA release from presynaptic inhibitory neurons expressing cannabinoid receptors (adapted with permission from ref. 65). Intrinsic membrane properties of the GCaMP6m-expressing CA3 cells were similar to previously reported values for CA3 (ref. 66); mean resting potential: -72.1 ± 1.6 mV; mean input resistance: 161.8 ± 26.4 MΩ; $n = 7$. **b**, Sample trace illustrating DSI of sIPSCs in a GCaMP6m-expressing CA3 cell following application of a depolarizing current step (from -65 mV to 0 mV for 500 ms). **c**, Sample trace illustrating lack of DSI of sIPSCs with inclusion of the intracellular calcium chelator BAPTA (1,2-bis(o-aminophenoxy)ethane-N,N,N',N'-tetraacetic acid) in the patch pipette. **d**, Summary graph of normalized charge transfer in GCaMP6m-expressing cells with standard intracellular solution (left, normalized charge transfer of sIPSCs following DSI

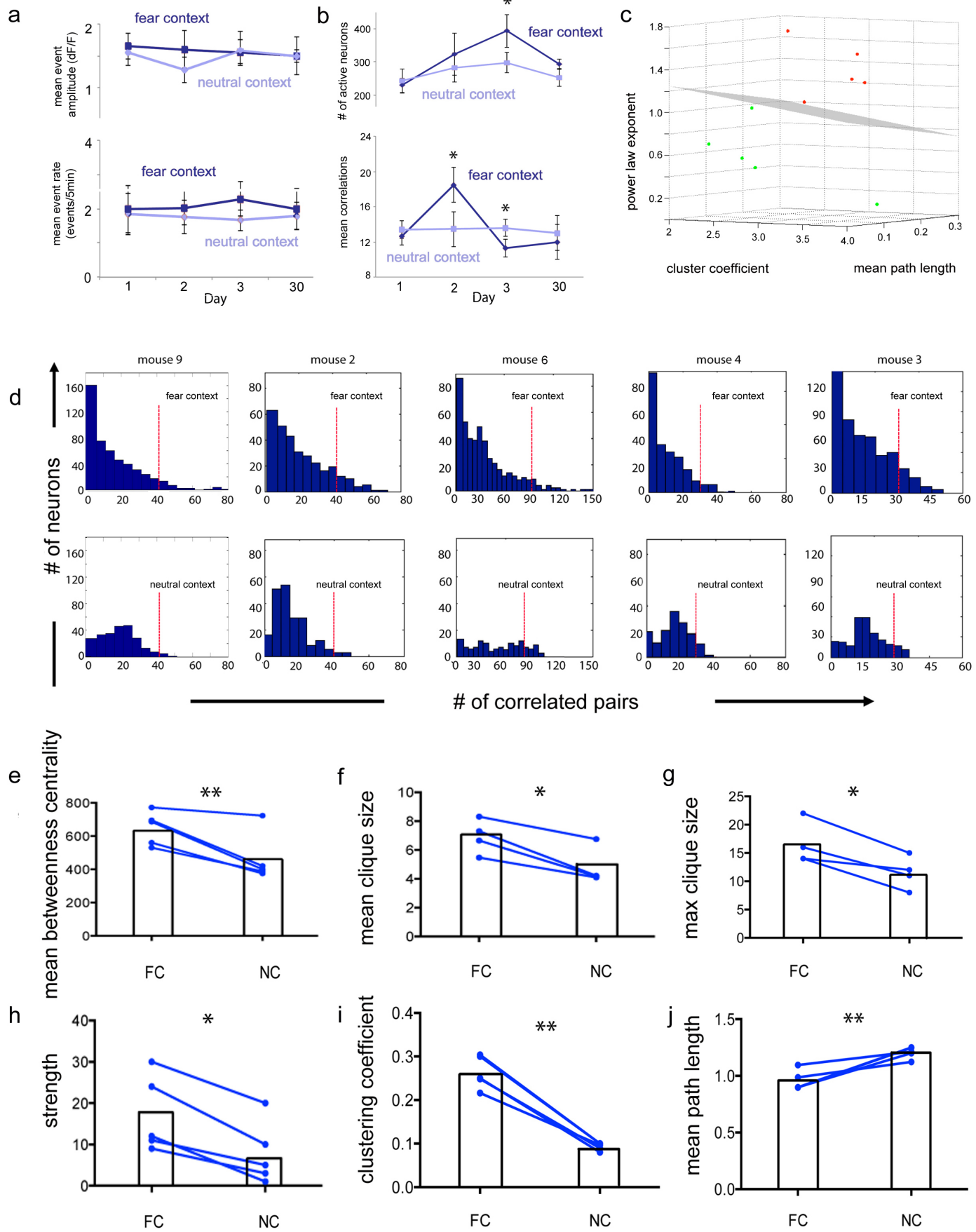
compared with pre-pulse baseline over the same fixed interval: charge reduced to $46.9 \pm 6.7\%$ of baseline charge; $n = 7$; comparable to charge transfer reported for non-GCaMP-expressing cells⁶⁷ and with addition of intracellular BAPTA (right, $n = 6$; error bars represent standard error of the mean (s.e.m.); $P < 0.05$, paired *t*-test). **e**, Spontaneous event rate (detection described in Methods) of GCaMP6m-expressing neurons as a function of baseline GCaMP6m fluorescence intensity (arbitrary units spanning the range over which event-rate population data could be reliably quantified) in each cell (pooling all neurons with ≥ 1 significant transient, from all mice, over all fields of view). Event rates were not observed to change significantly as a function of GCaMP6m expression level (Spearman's rank correlation coefficient: 0.48, $P = 0.3$). **f**, Behavioural scores from mice before GCaMP6m virus injection and implantation of cannulae above hippocampus; lick rates for the first 2 min in the fear (black) versus neutral (grey) contexts are provided. The level of learning assessed by lick suppression on day 3 retrieval (mean 0.5 ± 0.3 for day 3 fear versus 2.7 ± 0.3 for day 3 neutral; $n = 10$, $P < 0.001$, paired *t*-test) pre-injection/implantation was comparable to levels corresponding to post-injection/implantation (compare with Fig. 3b). * $P < 0.05$, ** $P < 0.01$, *** $P < 0.001$.



Extended Data Figure 4 | Real-time imaging of neural ensembles in three-dimensional hippocampal volumes: extraction of neural sources and identification of significant transients. **a**, Head-fixed virtual reality setup. Mice run on an axially fixed track ball³¹ while movements and licking behaviour are measured through an optical mouse and a lickometer, respectively, both interfaced with the virtual-reality gaming software. For contextual fear conditioning, water-restricted mice were exposed to two contexts with distinct visual, olfactory, tactile and auditory cues (day 1), and provided with aversive air puffs in one context (fear context), but not the other (neutral context) (day 2). Fear memory retrieval in the two contexts was quantified (days 3, 30) by lick suppression. **b**, Sample mean intensity z projections from raw videos (scale bar: 50 μm), with extracted neural sources (segmented cells) from CA3 for each of the optical sections, along with the first 50 time-series traces. Scale: 300% $\Delta F/F$, 30 s. **c**, Identification of significant transients in $\Delta F/F$

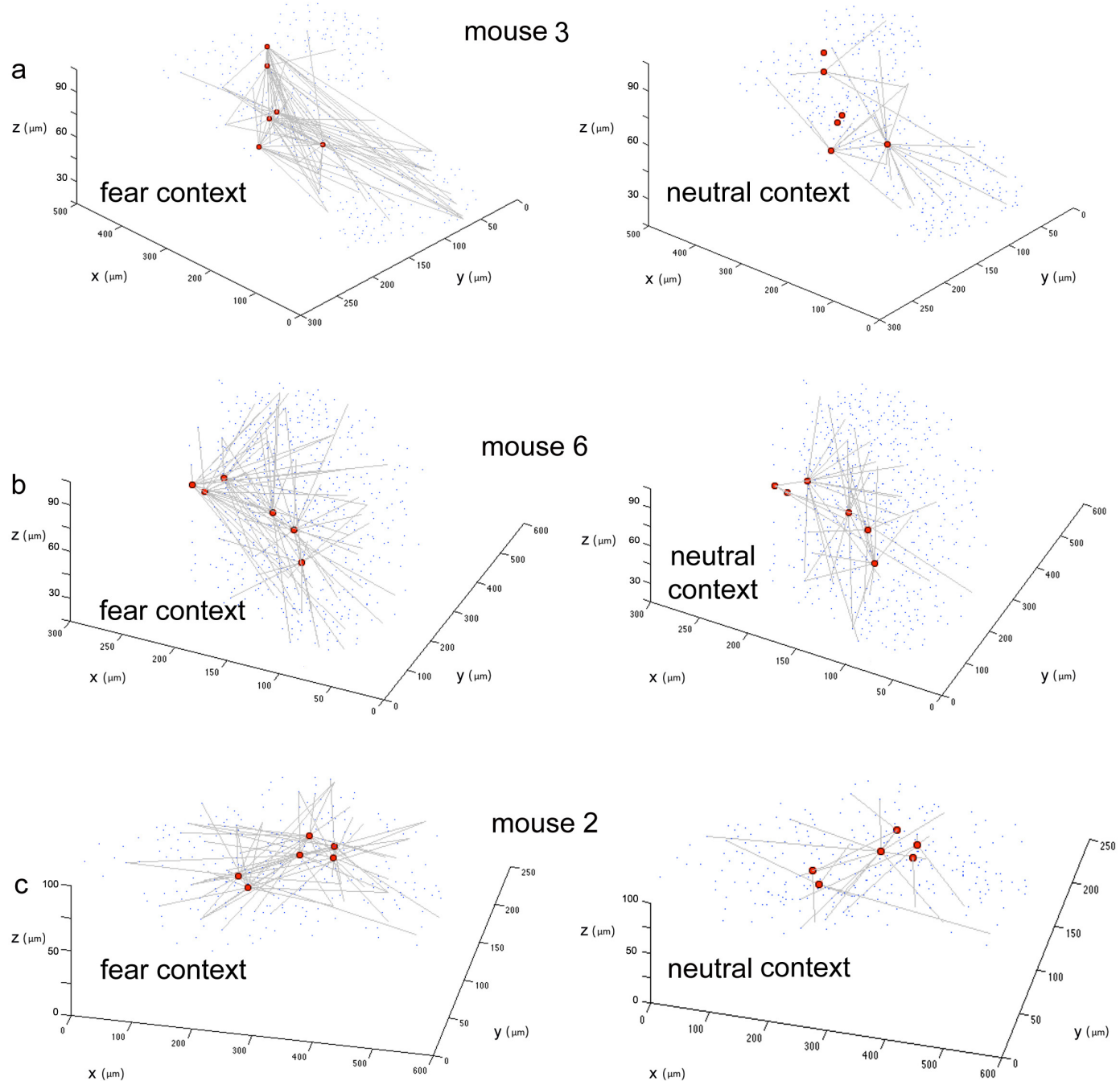
traces. Histogram showing the distribution of events occurring at amplitude 2σ above noise (noise calculated on a per-cell basis), over a range of event duration in seconds. The number of negative-going transients at each amplitude and duration are plotted in red to the left of the ordinate, and positive-going transients at each amplitude and duration are plotted in blue to the right.

d, e, The above analysis is repeated for events that occur at an amplitude of 3σ (**d**) and 4σ (**e**). **f**, False positive rates for 2-, 3-, and 4- σ events (pooled across all neurons in all mice over all FOVs). False positive rate curves were calculated for each σ level by dividing the number of negative events at that level by the number of positive events at that level (Methods). Event onset was defined as the time corresponding to $\Delta F/F$ exceeding 2σ , and offset as the time corresponding to $\Delta F/F$ falling below 0.5σ . A decaying exponential was fit by least-squares to the false positive rate values, allowing for the determination of a minimum transient duration at each σ level for different confidence levels.



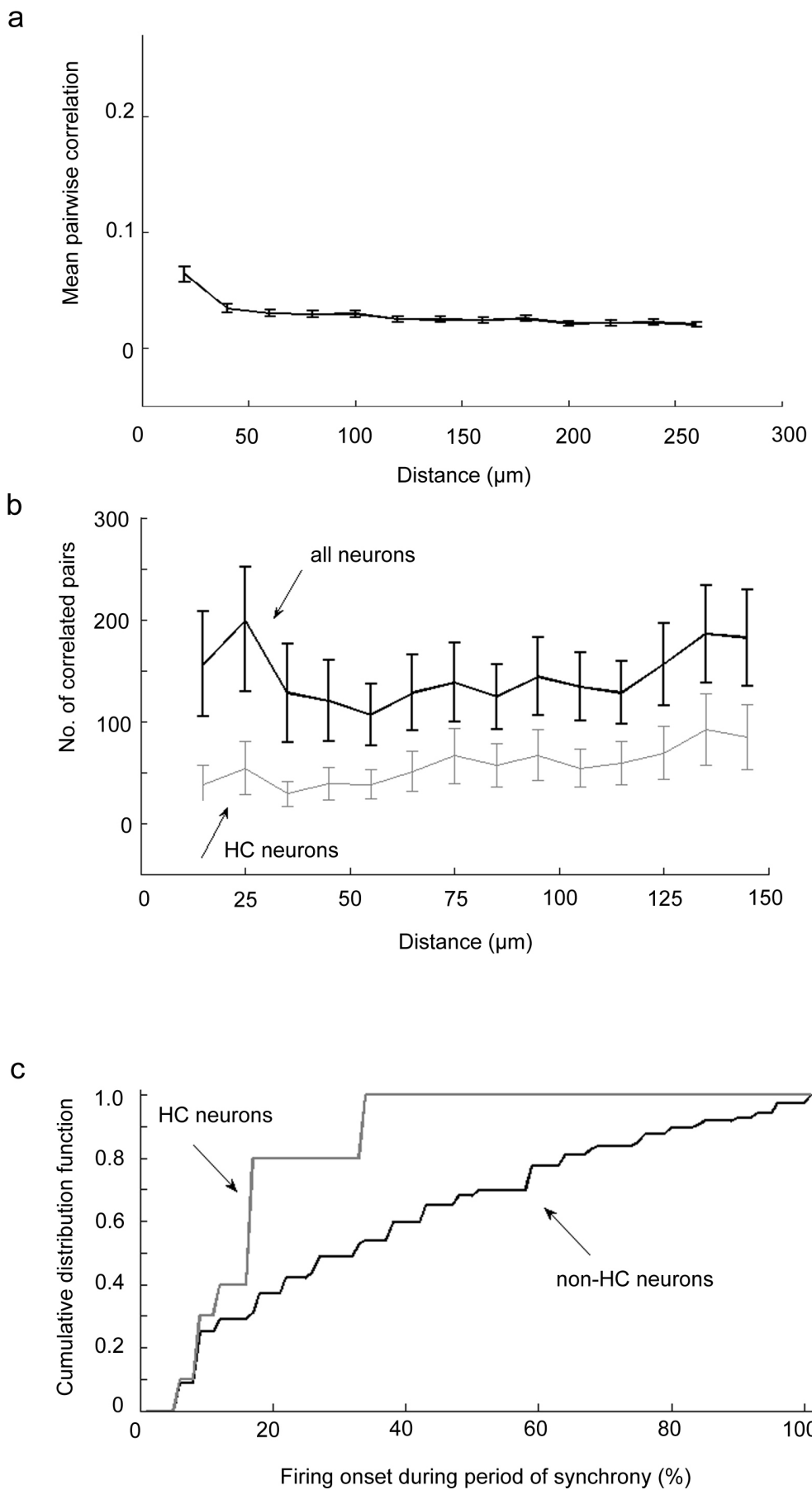
Extended Data Figure 5 | Cell populations and graph properties of fear and neutral networks in hippocampus during retrieval. **a**, No context-dependent change in total event amplitude or rate was detected. Top, mean GCaMP6m-detected event amplitude (average $\Delta F/F$ of all significant events; definition of significant event for each neuron as described in Methods) is plotted across days for mice in the fear and neutral contexts ($n = 5$ mice, not significant in paired t -tests). Bottom, mean GCaMP6m-detected event rate plotted across days for mice in the fear and neutral contexts ($n = 5$ mice, not significant in paired t -tests). **b**, Context-dependent changes in individual-neuron and correlated behaviour were observed. Top, number of active neurons (at least one significant GCaMP6m transient detected within first 2 min in context) plotted for fear and neutral contexts ($n = 5$ mice, 378 ± 64 for day 3 fear context versus 257 ± 39 for day 3 neutral context; $P < 0.05$, paired t -test, mean \pm s.d.). Bottom, mean number of correlated pairs per neuron (where pairwise Pearson's correlation coefficient >0.3) plotted for fear and neutral contexts ($n = 5$ mice, 18.5 ± 1.8 for day 2 fear context versus 13.4 ± 1.4 for day 2 neutral context; 11.3 ± 0.8 for day 3 fear context versus 13.6 ± 0.5 for day 3 neutral context; $P < 0.05$, paired t -test). **c**, Fitting histograms from Fig. 3d to an exponential distribution of the form ae^{-bx} demonstrates a power-law ($b > 1$) distribution in day 3 fear context (each red dot represents one mouse) compared to day 3 neutral context ($b < 1$; green dots), which was consistent across all mice ($n = 5$ mice; $P < 0.01$, paired t -test). Many graph

properties were calculated for fear versus neutral context, but the power-law exponent of the degree distribution distinguished fear (red) from neutral (green) most powerfully (discriminants shown: coefficient of the power law exponent = 0.78, coefficient of cluster coefficient = 0.61, coefficient of mean path length = 0.11, with 90% confidence intervals being [0.74, 1.0], [0.1, 0.65] and [0.01, 0.23], respectively). These confidence intervals were obtained using 1,000 bootstrapped samples; shown is the best three-dimensional hyperplane separation using a linear support vector machine classifier. **d**, Histograms of the number of correlated partner neurons existing for each neuron in fear versus neutral context on day 3 (retrieval testing) across mice. The dotted red line indicates correlation threshold (set automatically as mean + 1 standard deviation in the number of correlated pairs in the network), to the right of which lie (by definition) the highly correlated or HC neurons. Similar measurements of interest in fear versus neutral context across mice were calculated and are provided here for other graph invariant properties: **e**, betweenness centrality; **f, g**, clique properties; **h**, strength; **i**, cluster coefficient; and **j**, mean path length (all defined in Methods). For the above calculations, correlation between two neurons was defined to exist when the pairwise Pearson correlation coefficient exceeded 0.3 (Methods). Data are presented as individual data points corresponding to each mouse, with mean \pm s.d. * $P < 0.05$, ** $P < 0.01$, *** $P < 0.001$, using paired t -tests.



Extended Data Figure 6 | Functional relationships of fear-context-defined HC neurons as appearing in fear versus neutral context. **a–c**, Data from all additional mice (beyond the exemplar of Fig. 3e, f) demonstrating that HC neurons (red circles) in the fear context with a high degree of correlated partners (grey edges) when located in the neutral context have a much lower degree of correlated partners ($n = 4$ mice including the example in Fig. 3e, f);

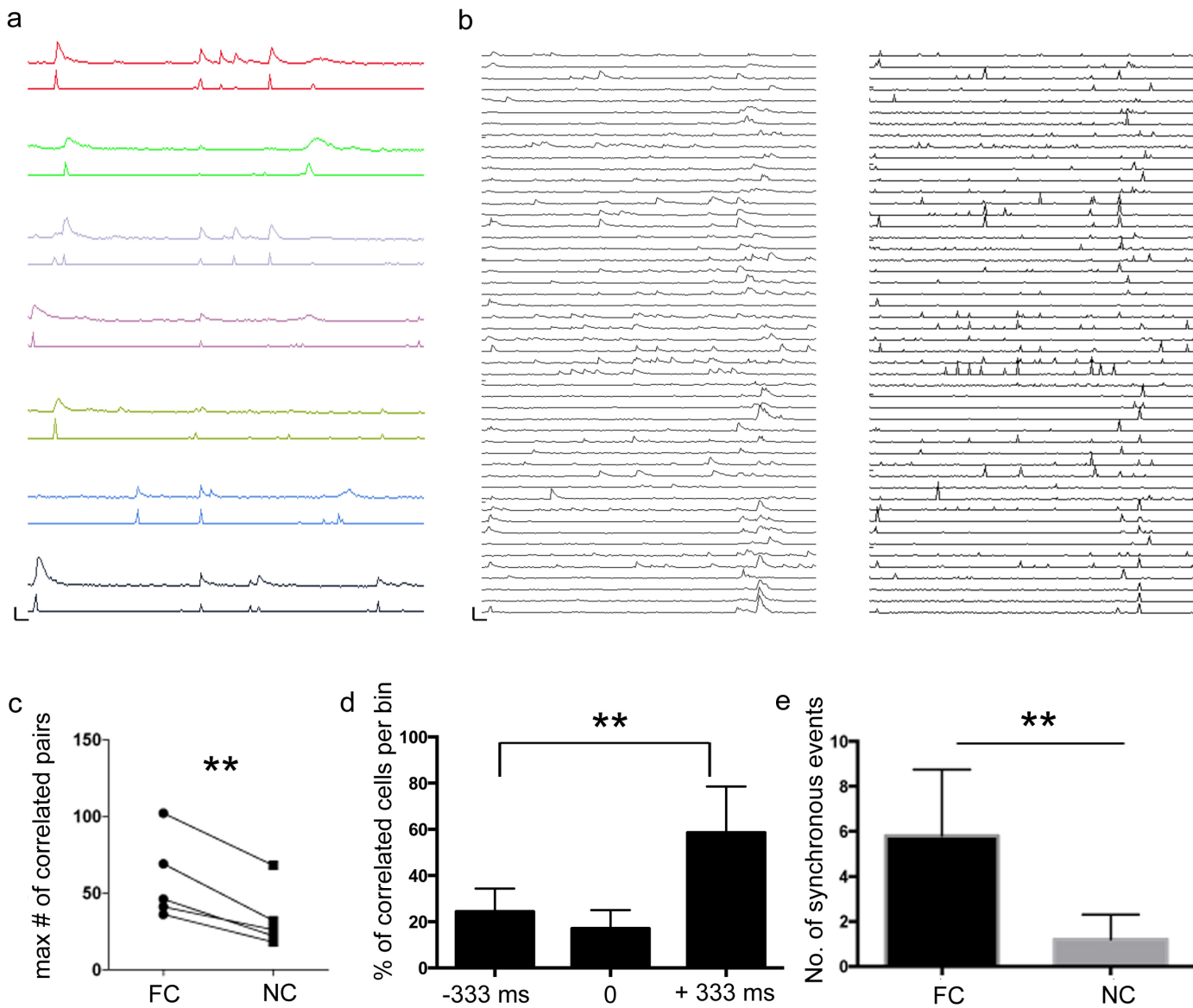
mean = 60 correlated pairs (standard deviation 19.4) in fear context versus mean = 18 correlated pairs (standard deviation 14.2) in neutral context; $P < 0.01$ by paired *t*-test). Only four mice are analysed here because the exact same FOV (with cell identities) was not captured in fear versus neutral context for one mouse.



Extended Data Figure 7 | Spatial and temporal organization of HC neurons.

a, Plot of mean pairwise correlation versus mean pairwise distance averaged over all FOVs (all days and all contexts) from all five mice. It was possible to detect a significant but weak relationship between mean correlation and distance (Spearman's correlation = -0.66 , $P = 0.01$), which could be a reflection of fine-scale spatial clustering as might be expected of recurrent circuits in CA3, but would also probably include residual crosstalk between regions of interest (ROIs) due to brain motion and common neuropil signal, which is expected and not significantly different from what has been previously observed in the hippocampus³. **b**, Plot of the number of correlated pairs versus pairwise distance for all neurons (black line), and HC neurons only (grey line). More correlated pairs were found at greater distances for HC

neurons (Spearman's = 0.84 , $P = 0.002$ for HC neurons; Spearman's correlation = 0.23 , $P = 0.43$ for all neurons). **c**, Cumulative distributions showing fraction of HC neurons (*y*-axis) with onset times at various latencies across the time course of synchronous events (*x*-axis) averaged across all mice, compared to response latencies of non-HC neurons. HC neuron activity appeared significantly earlier than for non-HC neurons during synchronous events ($P < 0.001$, Kolmogorov–Smirnov two-tail test, $\kappa = 0.664$; note the horizontal resolution of the plot is inversely proportional to length of the synchrony window, and dependent on frame duration; for instance, a 10-s-long synchrony window with frame duration of 333 ms corresponds to a 3.33% resolution per frame).

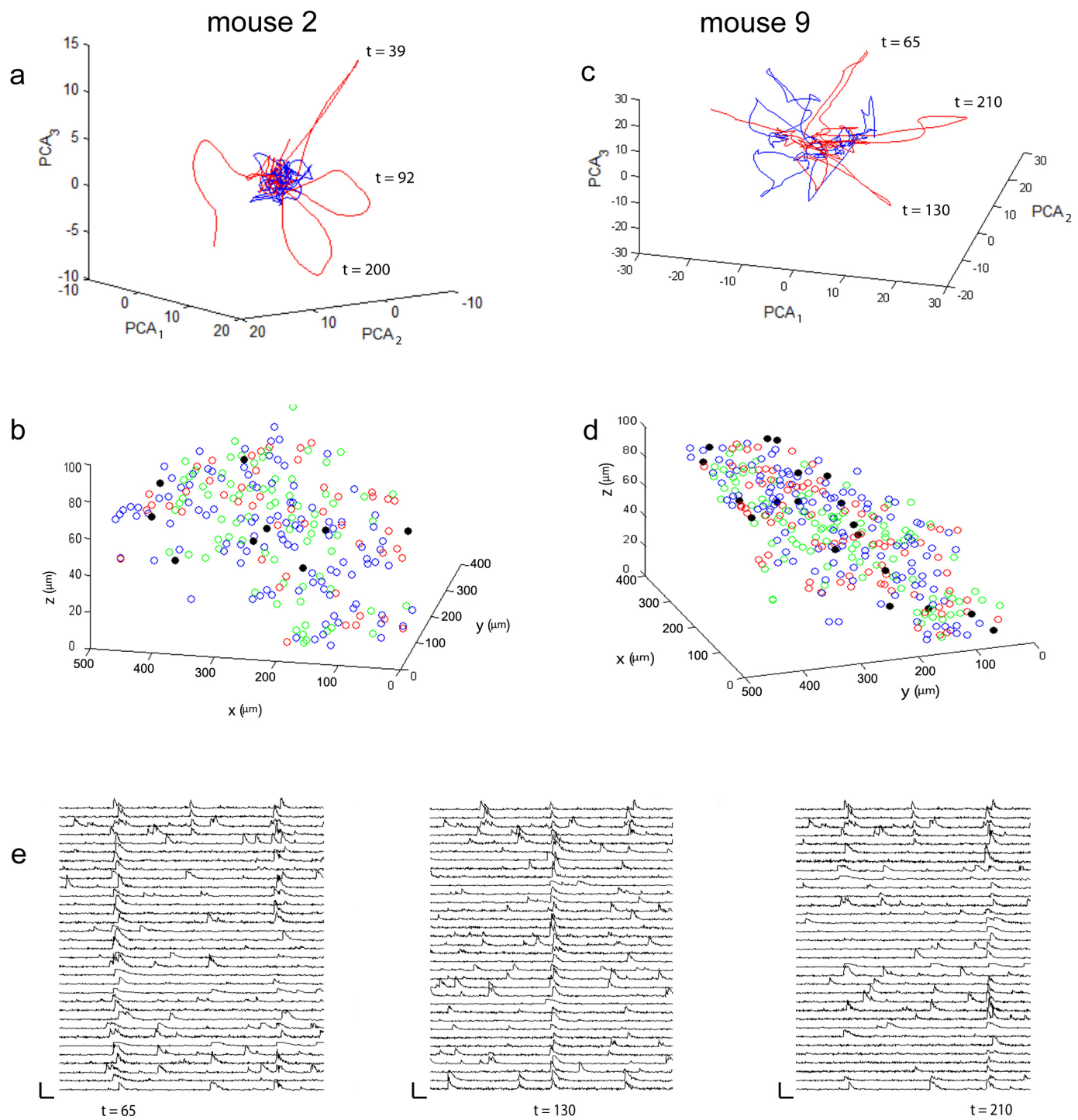


Extended Data Figure 8 | Additional analyses: estimation of event onsets using fast non-negative deconvolution, and correlated pair analysis.

a, Example pairings of the original GCaMP6m trace (top traces), with the deconvolved trace (bottom traces), shows reliable estimation of event onset from deconvolved data (deconvolution algorithm and parameters detailed further in Methods). Scale bar: 150% $\Delta F/F$, 10 s. **b**, Original GCaMP6m traces from a representative synchronous event in one animal (left), paired with the deconvolved traces for that same synchronous event (right). Scale bar: 300% $\Delta F/F$, 10 s. **c**, The highest-degree node (neuron with the greatest number of correlated pairs) in the day 3 fear context had significantly more correlated pairs than the highest degree node in the day 3 neutral context, significant

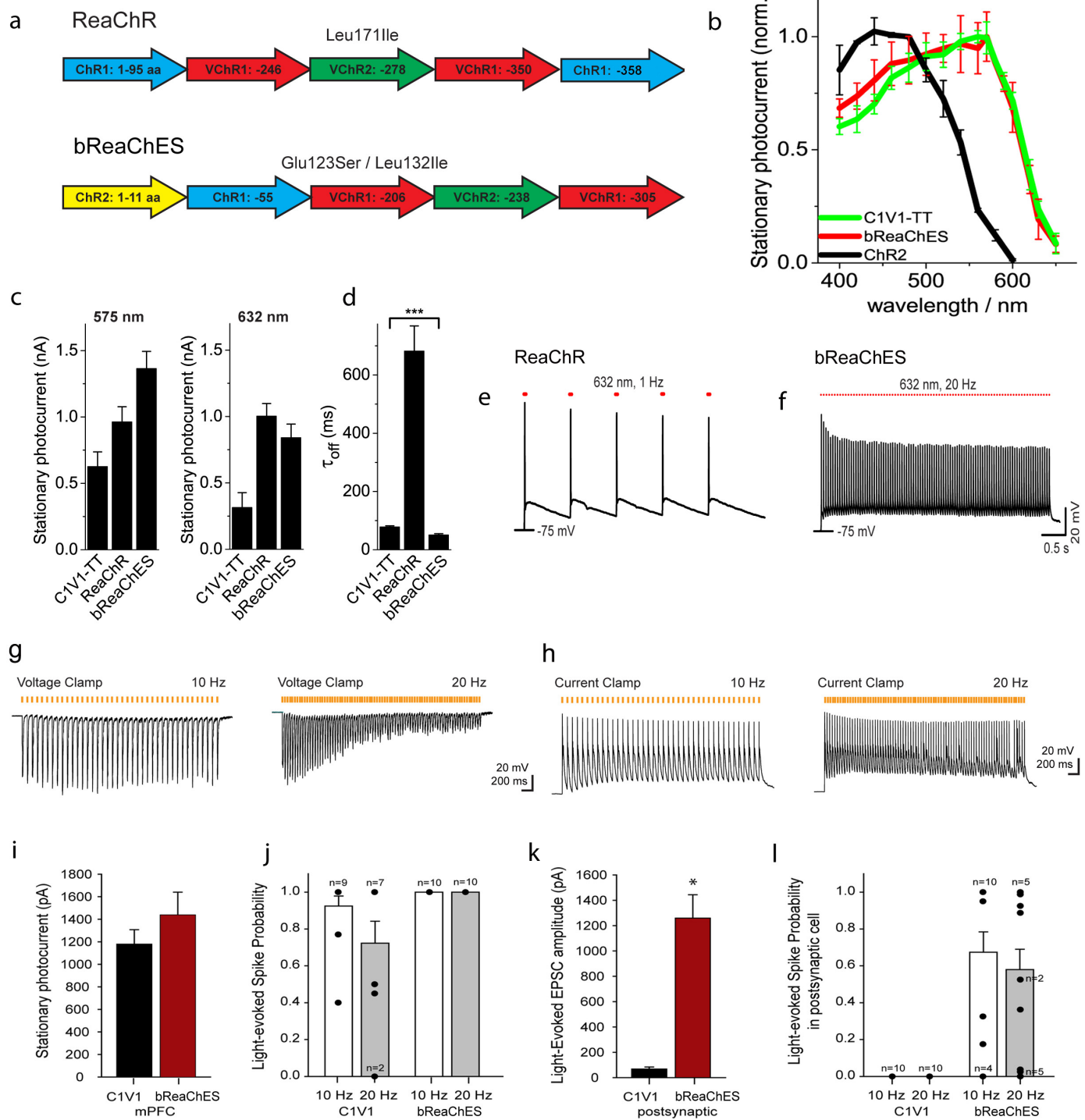
across $n = 5$ mice (58.8 versus 33.2 pairs, $P < 0.01$, paired t -test). **d**, Temporal relationship of HC neuron activity onset (set to time 0) compared with onset activity of correlated pairs (binned into 333 ms preceding or succeeding HC activity); $n = 48$ HC neurons. HCs were more likely to lead than lag their correlated pairs ($58.5 \pm 20\%$ leading versus $24.4 \pm 10\%$ lagging; $P < 0.01$, unpaired t -test). **e**, Significant synchronous activity (defined in Methods) quantified across five mice: number of synchronous events in the fear context was significantly greater than in the neutral context (5.8 \pm 2.9 events in fear context versus 1.2 \pm 1.1 in neutral context; $P < 0.01$, paired t -test).

* $P < 0.05$, ** $P < 0.01$, *** $P < 0.001$.



Extended Data Figure 9 | PCA of population trajectories in fear versus neutral contexts. **a**, PCA of $\Delta F/F$ traces of all active cells for mouse 2, performed separately for fear and neutral contexts. Population trajectories in the fear context take large, nearly orthogonal, deviations from the centre, while neutral context trajectories remain close to the origin. **b**, Three-dimensional reconstruction of the neuronal population showing that neurons participating in each synchronous event (red cells ($t = 39$), green circles ($t = 92$), blue circles

($t = 200$)) are largely non-overlapping and anatomically homogeneously distributed throughout the volume. There are, however, a small fraction of neurons that participate in all three events (black circles). **c, d**, Data are shown for another representative mouse. Similar results were seen in all other mice. **e**, The $\Delta F/F$ traces for a randomly selected set of 30 neurons participating in each of three events are shown, with the greatest amount of overlap seen between $t = 65$ and $t = 210$. Scale bars: 400% $\Delta F/F$, 20 s.



Extended Data Figure 10 | bReaChES: engineering a red-shifted opsin for robust projection targeting. **a**, Schematics of ReaChR³¹ and bReaChES. ReaChR is a hybrid of segments from channelrhopsin-1 (blue, amino acids 1–95), *Volvox* channelrhodopsin-1 (red, amino acids 96–246, 279–350) and *Volvox* channelrhodopsin-2 (green, amino acids 247–278). The VChR1 segment contains the point mutation Leu171Ile. ReaChR was modified here for enhanced expression and membrane trafficking as well as accelerated channel kinetics, resulting in bReaChES, as follows. The first 51 amino-terminal residues were replaced by the first 11 amino-terminal residues from channelrhodopsin-2 (yellow, amino acids 1–11) and the last 5 carboxy-terminal residues were removed. Mutation of Glu 123 to Ser increases speed of channel closure. **b**, Spectra of C1V1_{TT}, bReaChES and ChR2 measured between 400 and 650 nm at 0.65 mW mm⁻² in cultured neurons from rat hippocampus ($n = 6$ each). **c**, Stationary photocurrents at 575 nm (C1V1_{TT} 630 ± 109 pA (s.e.m. throughout figure), ReaChR 963 ± 113 pA, bReaChES 1,365 ± 128 pA) and 632 nm (C1V1_{TT} 315 ± 111 pA, ReaChR 1,003 ± 95 pA, bReaChES 841 ± 102 pA). Current amplitudes were measured at −80 mV

and 5 mW mm⁻² light intensity, respectively. **d**, Speed of channel closure: τ value of mono-exponential off-kinetics (C1V1_{TT} 79 ± 3.7 ms, $n = 26$; ReaChR 682 ± 86 ms, $n = 6$; bReaChES 49 ± 4.4 ms, $n = 25$; $P < 0.0005$). **e, f**, Representative current-clamp traces of ReaChR- or bReaChES-expressing cultured neurons excited with 633 nm light (5 ms, 5 mW mm⁻²). ReaChR kinetics were slow enough that reliable action potential generation was only possible at very low frequencies (**e**), while the accelerated channel closure of bReaChES allowed reliable spike generation up to 20 Hz (**f**). **g, h**, Representative voltage-clamp (**g**) and current-clamp (**h**) traces of postsynaptic cells responding to light stimulation (orange) of bReaChES-expressing presynaptic terminals. Pulse length: 5 ms. **i, j**, Stationary photocurrents (**i**) and light-evoked spike probability (**j**) in opsin-expressing medial PFC (mPFC) cells in acute slice (C1V1_{TT}: $n = 11$, bReaChES: $n = 10$). **k, l**, Light-evoked EPSC amplitude (**k**) and spike probability (**l**) in postsynaptic cells (C1V1_{TT}: $n = 10$, bReaChES: $n = 18$). Light wavelength 575 nm (25 nm bandwidth) and power density 5 mW mm⁻². * $P < 0.05$, ** $P < 0.01$, *** $P < 0.001$.